Technical Memo

ECMWF
European Centre for Medium-Range Weather Forecasts

880

Evaluation of ECMWF forecasts, including the 2020 upgrade

T. Haiden, M. Janousek, F. Vitart,
Z. Ben Bouallegue, L. Ferranti, F. Prates
and D. Richardson

(Forecast Department)

January 2021

Series: ECMWF Technical Memoranda

A full list of ECMWF Publications can be found on our website under:
http://www.ecmwf.int/en/publications

Contact: library@ecmwf.int

European Centre for Medium-Range Weather Forecasts, Shinfield Park, Reading, RG2 9AX, UK

The information within this publication is given in good faith and considered to be true, but ECMWF accepts no liability for error or omission or for loss or damage arising from its use.

1 Introduction

The most recent change to the ECMWF forecasting system (IFS Cycle 47r1, on 30 June 2020) is summarised in section 2. The description of changes and meteorological impacts from this upgrade largely follows the ECMWF Newsletter article of Sleigh et al. (2020). Verification results of the ECMWF medium-range upper-air forecasts are presented in section 3, including, where available, a comparison of ECMWF's forecast performance with that of other global forecasting centres. Section 4 presents the verification of ECMWF forecasts of weather parameters and ocean waves, while severe weather is addressed in section 5. Finally, section 6 discusses the performance of monthly and seasonal forecast products.

As in previous reports a wide range of verification results is included and, to aid comparison from year to year, the set of additional verification scores shown here is consistent with that of previous years (ECMWF Tech. Memos. 346, 414, 432, 463, 501, 504, 547, 578, 606, 635, 654, 688, 710, 765, 792, 817, 831, 853). A few new plots have been included to highlight additional aspects of ECMWF's forecast performance. A short technical note describing the scores used in this report is given at the end of this document.

Verification pages are regularly updated, and accessible at the following address:

www.ecmwf.int/en/forecasts/charts

by choosing 'Verification' under the following headers

- 'Medium Range' (medium-range and ocean waves)
- 'Extended Range' (monthly)
- 'Long Range' (seasonal)

2 Changes to the ECMWF forecasting system

2.1 Meteorological content of IFS Cycle 47r1

On 30 June 2020, ECMWF implemented a substantial upgrade of its Integrated Forecasting System (IFS). IFS Cycle 47r1 includes changes in the forecast model and in the data assimilation system. The upgrade has had a small positive impact on forecast skill in the medium and extended range in the troposphere, and a large positive impact on analyses and forecasts in the stratosphere. The latter is mainly due to reduced large-scale biases. Cycle 47r1 brings changes in many areas, including:

In data assimilation: revised model error in weak-constraint 4D-Var data assimilation; situation-dependent skin temperature background error variances from the Ensemble of Data Assimilations (EDA); shorter time step in the last 4D-Var minimisation; first guess in delayed cut-off 12-hour 4D-Var obtained from 8-hour Early Delivery Data Assimilation.

In the use of observations: revised ATMS (Advanced Technology Microwave Sounder) observation errors; spline interpolation introduced in the 2D GPS-RO (radio occultation) bending angle operator.

In the model: quintic vertical interpolation in semi-Lagrangian advection; modified Charnock parameter for high wind speeds in tropical cyclones; 6-component MODIS (Moderate Resolution Imaging Spectroradiometer) albedo over land.

2.1.1 Data assimilation

In Cycle 47r1, the covariances controlling the model bias estimate in weak-constraint 4D-Var have been revised. The previous weak-constraint 4D-Var corrected only a small fraction of the model bias above 40 hPa, while the revised weak-constraint implementation better corrects the diagnosed cold and warm biases of the model above 100 hPa, reducing the mean error by up to 50%. Results show that biases in the upper stratosphere between 11 hPa and 1.5 hPa are also significantly reduced in the new system. For more details, see Laloyaux and Bonavita (2020).

Another important contribution to Cycle 47r1 is a change in the estimate of the background error variance for skin temperature over land, from constant values to spatially varying, situation-dependent variances derived from the EDA. This affects the assimilation of microwave and infrared (IR) radiance observations of the mid- and lower troposphere, which typically contain a contribution of radiation emitted from the surface. The EDA estimate was activated over land surfaces initially, where the magnitude of skin temperature errors can be very heterogeneous in space and time.

The time step in the last 4D-Var minimisation has been reduced in this new cycle from 900 seconds to 450 seconds. With this change, the inner loop and outer loop time steps match. This avoids different gravity wave speeds between the tangent-linear model (used in the computation of the final increment as part of the last inner loop) and the nonlinear model (outer loop). In the semi-implicit advection scheme of the IFS, the gravity wave speed depends on the time step. The change brings multiple benefits: clear improvements to stratospheric analyses and forecasts, and a smaller but statistically significant impact on tropospheric skill; monotonic convergence of incremental 4D-Var in some atmospheric situations, such as sudden stratospheric warming events; and an improved initial balance of the 4D-Var analysis.

The concept of continuous data assimilation introduced in Cycle 46r1 has been extended by using the analyses from each 8-hour Early Delivery Data Assimilation (DA) window as first guesses for the 12-hour Long-Window Data Assimilation (LWDA). From Cycle 47r1, the LWDA analysis can be viewed as a time extension of the DA analysis. There is no change in the background state for the LWDA, but the first minimisation is provided with a more accurate starting point. For more details, see Hólm et al. (2020).

As a result of this change, the analysis increments in LWDA increase, mainly due to the fact that more information is extracted from observations. This leads to an apparent degradation of forecasts when they are verified against own analyses. In reality, forecasts have not deteriorated but the analysis against which they are assessed has changed. When verified against an independent analysis, like reanalysis, the impact on forecast skill from this change is neutral overall. An important benefit of this change is that it allows 4D-Var to more effectively initialise non-linear processes. Short-range forecasts are closer to observations in particular for observations which are more non-linearly related to the model state, such as radiances sensitive to water vapour, cloud and precipitation.

2.1.2 Use of observations

The use of hyperspectral IR data (AIRS, IASI, CrIS instruments) has been enhanced in Cycle 47r1 by allowing high-peaking channel radiances to be assimilated in locations where lower-peaking channels are rejected due to aerosol contamination. Up to Cycle 46r1, the aerosol detection scheme rejected entire IR spectra if aerosol was detected in any channel. The number of assimilated IR observations has increased by up to 5% for stratospheric channels due to this enhancement. The change is most effective in regions where aerosol (particularly Saharan dust) occurs most frequently.

In Cycle 47r1, a consistent formulation of the inter-channel error correlations was introduced for ATMS from the Suomi-NPP and NOAA-20 satellites. This change results in small but consistent improvements to first-guess fits to independent observations such as AMSU-A and the IR humidity sounding channels, indicating improved short-range forecasts of tropospheric temperature and humidity.

From Cycle 47r1, a bilinear interpolation replaces the nearest-neighbour interpolation in the computation of forecast departures for all-sky microwave radiance observations for most variables. These include temperature and humidity but not cloud hydrometeors and not the land–sea mask, for which nearest-neighbour interpolation is preferable. This change results in significantly improved first-guess fits to all-sky microwave imager and sounder radiances.

In Cycle 47r1, an improved interpolation approach has been introduced in the GPS-RO observation operator for bending angles. This revision of the interpolation ensures that refractivity gradients are continuous in the vertical and produce more realistic profiles of bending angle variability. The change leads to a small increase in the standard deviation of GPS-RO first guess departures due to the intended increase in variability, but the analysis departures are slightly improved.

2.1.3 Model changes

In Cycle 47r1, the advection of temperature and humidity has been changed by increasing the order of the vertical interpolation in the semi-Lagrangian scheme from three to five. This quintic interpolation in the semi-Lagrangian advection alleviates an unphysical cooling of the IFS model in the stratosphere at high horizontal resolution. The change and its impact are described in detail in Polichtchouk et al. (2020).

A number of improvements have been made to the specification of the shortwave albedo of the land surface, snow and sea ice. The land-surface albedo is based on a monthly climatology derived from the MODIS instrument. Until Cycle 46r1, it consisted of separate albedos for direct and diffuse solar radiation in two spectral regions: ultraviolet/visible, and near-IR. Albedo for direct solar radiation was computed assuming an overhead sun, for which albedo is systematically lower than for other sun angles. In Cycle 47r1, the dependence of the direct albedo on solar zenith angle is represented following Schaaf et al. (2002). This requires six climatological fields, three in each of the two spectral regions. This tends to increase the albedo of snow-free land surfaces, on average. In addition, the albedo for the 0.625–0.778 μm band of the shortwave radiation scheme has been determined by a weighted average of the MODIS albedos for the ultraviolet/visible and the near-IR, instead of using the latter only. The improved albedo for this spectral band justified the removal of an artificial adjustment of the limits of the prognostic snow albedo, and the introduction of spectrally varying snow albedos consistent with MODIS observations as reported by Moody et al. (2007). These changes warm summer land areas in the model by around 0.1˚C and by up to 0.3˚C over North Africa, primarily due to the darkening of the land surface from the recomputed albedo in the 0.625–0.778 μm band. There is a small reduction in the root-mean-square error of temperature forecasts, which stems from a reduction in the model's cold bias in 2-metre temperature in many regions. A clear improvement in daytime temperature forecasts over the Sahara has been observed.

Two additional changes were made in the treatment of radiation: (i) the time series of total solar irradiance has been updated using data from Matthes et al. (2017), which include the 11-year solar cycle and are consistent with the latest solar measurements; (ii) the time series of concentrations of greenhouse gases have been updated (CMIP6's SSP3-7.0 / option 2). There is no detectable impact of (i) on forecasts, while (ii) slightly warms the upper stratosphere in analyses and forecasts in present-day simulations because in Cycle 47r1 CO_2 concentrations are consistent with recent measurements and slightly lower than previously used estimates of CO_2 concentrations.

The parametrization of momentum exchange with the ocean surface has been changed in Cycle 47r1. The relationship is expressed in a wind-speed-dependent drag coefficient. A considerable reduction of the drag under very strong winds (above 33 m/s) has been introduced. This change of drag over the ocean at high wind speeds yields a substantial improvement in maximum 10-metre wind speeds in intense tropical cyclones (Bidlot et al., 2020).

Minor changes have been made in the convection scheme in Cycle 47r1. They involve stability corrections to the mid-level and deep convective closures and reduced bounds for parcel perturbations. Furthermore, the convective inhibition diagnostic (CIN) has been revised to use virtual potential temperature instead of equivalent potential temperature. The revised CIN is now much reduced and is closer to values expected by forecasters.

2.2 Meteorological impact of the new cycle

Figure 1 and Figure 2 show score changes and their statistical significance for the high-resolution forecast (HRES) and the ensemble forecast (ENS), respectively. HRES is run at TCo1279 resolution (corresponding to a horizontal grid spacing of about 9 km) and ENS at TCo639 (corresponding to a horizontal grid spacing of about 18 km).

The new cycle brings improvements throughout the troposphere of the order of 0.5% in extratropical forecasts. The improvements are most apparent in ENS scores, both against own analysis and against observations. In the extratropical stratosphere, the new cycle brings large improvements, such as 2–5% error reductions for temperature and geopotential at 100 hPa, and 5–15% at 50 hPa. In the tropics, there is an apparent degradation of 1–3% in upper-air scores when forecasts are verified against the new cycle's own analyses. This does not reflect any change for the worse in the forecasts but is the result of changes to the analysis, as described above. Verification against observations shows that upper-air changes in the tropics are neutral overall, with small improvements and deteriorations balancing each other out. One exception is 250 hPa temperature in the tropics, where a deterioration of 1–3% is seen against observations. This is mainly due to a small (about +0.1 K) shift in the mean, resulting from the model changes.

The new cycle improves forecasts of several near-surface parameters, most notably 2-metre temperature and humidity (by about 0.5–1%) both in the extratropics and, when verified against observations, also in the tropics. Extratropical 10-metre wind in HRES is slightly improved, as well as total cloud cover in ENS and HRES. Tropical 10-metre wind and precipitation are slightly deteriorated. Significant wave height is mostly neutral against observations and improved against own analysis.

The impact of Cycle 46r1 on the model climate in the extended range (up to 46 days ahead) was generally neutral. By contrast, Cycle 47r1 has a significant positive impact in the lower stratosphere, with a decrease of the cold bias in the tropics at around 50 hPa. The impact of Cycle 47r1 on weekly mean anomalies is neutral, except for some improvement in 50 hPa meridional wind, and a small but statistically significant degradation in week 1 in the tropics for upper-level fields. The degradation in the fair CRPSS is consistent with a slight reduction of ensemble spread in week 1 over the tropics.

In addition to monitoring the evolution of probabilistic forecast skill scores in the scorecards, it is important to monitor the predictive skill of sources of sub-seasonal predictability, such as the Madden–Julian Oscillation (MJO). The difference in MJO bivariate correlation between Cycle 47r1 and Cycle 46r1 is not statistically significant. However, in Cycle 46r1, the MJO was too weak compared with the ERA5 reanalysis (by about 20% after day 15), and Cycle 47r1 weakens the MJO further by 3–4% in the extended range.

The seasonal forecast is not changed with Cycle 47r1. Nevertheless, the impact of the model upgrade on the model climate has been evaluated in lower-resolution seasonal forecasts. The most marked impact on the model climate in the seasonal range comes from introducing quintic vertical interpolation. This warms the equatorial and winter-hemisphere model climate stratosphere by about 0.5 K from the tropopause throughout the lower stratosphere, reducing the cold bias. Changes to the model physics have resulted in a small increase in precipitation in the Intertropical Convergence Zone (ITCZ) year-round. Longstanding biases in boreal summer zonal 10 m wind in the Indian Ocean increase slightly, worsening eastern equatorial Indian Ocean sea-surface temperature biases.

3 Verification of upper-air medium-range forecasts

3.1 ECMWF scores

Figure 3 shows the evolution of the skill of the high-resolution forecast of 500 hPa height over Europe and the extratropical northern and southern hemispheres since 1981. Each point on the curves shows the forecast range at which the monthly mean (blue lines) or 12-month mean centred on that month (red line) of the anomaly correlation (ACC) between forecast and verifying analysis falls below 80%. For the three domains shown, in 2019-20 the score has surpassed all previous 12-month values. This is mainly due to improvements from model cycle 46r1, which was implemented in June 2019 and described in detail in last year’s report (Haiden et al., 2019) and in the ECMWF Newsletter (Sleigh et al., 2019).

A complementary measure of performance is the root mean square (RMS) error of the forecast. Figure 4 shows RMS errors for both extratropical hemispheres of the six-day forecast and the persistence forecast. In both hemispheres, the 12-month running mean RMS error of the six-day forecast has reached its lowest values so far.

Figure 5 shows the time series of the average RMS difference between four- and three-day (blue) and six- and five-day (red) forecasts from consecutive days of 500 hPa forecasts over Europe and the northern extratropics. This illustrates the inconsistency between successive 12 UTC forecasts for the same verification time. Consistent with the decrease in RMS error (Figure 4), the 12-month running mean of this metric has continued its downward trend in both hemispheres.

The quality of ECMWF forecasts in the upper atmosphere in the northern hemisphere extratropics is shown through time series of temperature and vector wind scores at 50 hPa in Figure 6. Stratospheric scores benefitted less from model cycle 46r1 but are expected to show improvements due to 47r1, especially for temperature (see Figure 1).

The trend in ENS performance is illustrated in Figure 7, which shows the evolution of the continuous ranked probability skill score (CRPSS) for 850 hPa temperature over Europe and the northern hemisphere. At these relatively large lead times (around day 9), year-to-year variations in atmospheric predictability affect the score evolution more strongly than in the early medium-range. Unlike for the HRES, 12-month running mean values have not yet surpassed previous maxima, but there is a tendency for increased summer skill (seen as minima in the blue curve) in recent years. As soon as a winter season with higher predictability (such as 2016, 2017, or 2018) occurs, the year-round increase in skill will become more clearly apparent in the 12-month running mean values.

In a well-tuned ensemble system, the RMS error of the ensemble mean forecast should, on average, match the ensemble standard deviation (spread). The ensemble spread and ensemble-mean error over the extratropical northern hemisphere for last winter, as well as the difference between ensemble spread and ensemble-mean error for the last three winters, are shown in Figure 8. Both for 500 hPa geopotential height and 850 hPa temperature, forecasts show a good overall match between spread and error. For both parameters, the match between spread and error has improved overall in 2020 compared to 2019.

A good match between spatially and temporally averaged spread and error is a necessary but not a sufficient requirement for a well-calibrated ensemble. It should also be able to capture day-to-day changes in predictability, as well as their geographical variations. This can be assessed using spread-reliability diagrams. Forecast values of spread over a given region and time period are binned into equally populated spread categories, and for each bin the average error is determined. In a well-calibrated ensemble, the resulting line is close to the diagonal. Figure 9 and Figure 10 show spread-reliability plots for 500 hPa geopotential and 850 hPa temperature in the northern extratropics (top), Europe (centre), and the tropics (bottom, in Figure 10 only) for different global models. Spread reliability generally improves with lead time. At day 1 (left panels), forecasts are only moderately skillful in ‘predicting’ the average error, resulting in curves that deviate significantly from the diagonal, while at day 6 (right panels) most models are capturing spatio-temporal variations in error pretty well. Overall, ECMWF performs best, with its spread reliability closest to the diagonal. The stars in the plots mark the average values, corresponding to Figure 8, and ideally should lie on the diagonal, and as close to the lower left corner as possible. In this regard ECMWF performs best among the global models with the exception of 850 hPa temperature at day 1, where the Japan Meteorological Agency (JMA) forecast has the lowest error (although ECMWF has slightly better match between error and spread).

To create a benchmark for the ENS, the CRPS is also computed for a ‘dressed’ ERA5 forecast. This allows to better distinguish the effects of IFS developments from those of atmospheric variability and produces a more robust measure of ENS skill. The dressing uses the mean error and standard deviation of the previous 30 days to generate a Gaussian distribution around ERA5. Figure 11 shows the evolution of the CRPS skill of the ENS relative to the ERA5 reference for various upper-air parameters. Both at forecast days 5 (upper panel) and 10 (lower panel), the effect of 46r1 is clearly visible, leading to a forecast performance which is at its highest level so far.

The forecast performance in the tropics, as measured by RMS vector errors of the wind forecast with respect to the analysis, is shown in Figure 12. Both the 200 hPa and 850 hPa errors have decreased further and, more clearly visible in the day 5 curves, reached their lowest values. Scores for wind speed in the tropics are generally sensitive to inter-annual variations of tropical circulation systems such as the Madden-Julian oscillation, or the number of tropical cyclones.

3.2 WMO scores - comparison with other centres

The model inter-comparison plots shown in this section are based on the regular exchange of scores between WMO designated global data-processing and forecasting system (GDPFS) centres under WMO Commission for Observation, Infrastructure and Information Systems (Infrastructure Commission) auspices, following agreed standards of verification.

Figure 13 shows time series of such scores for 500 hPa geopotential height in the northern and southern hemisphere extratropics. Over the period shown, errors have decreased for all models, while ECMWF continues to maintain (at the 2-day range) or even slightly increase (at the 6-day range) the lead.

WMO-exchanged scores also include verification against radiosondes. Figure 14 (Europe), and Figure 15 (northern hemisphere extratropics), each showing 500 hPa geopotential height and 850 hPa wind forecast errors averaged over the past 12 months, confirm the leading performance of ECMWF medium-range forecasts relative to the other centres from day 2 onwards when verified against observations.

The WMO model intercomparison for the tropics is summarised in Figure 16 (verification against analyses) and Figure 17 (verification against observations), which show vector wind errors for 250 hPa and 850 hPa. When verified against the centres’ own analyses, the JMA forecast has the lowest error in the short range (day-2) while in the medium-range, both ECMWF and JMA are the leading models in the tropics. In the tropics, verification against analyses (Figure 16) is sensitive to details of the analysis method, in particular its ability to extrapolate information away from observation locations. When verified against observations (Figure 17), the ECMWF forecast has the smallest overall errors in the medium range. The positive effect of cycle 46r1 is not as strong in the tropics as in the extratropics. Improvements are smaller and only seen against observations.

4 Weather parameters and ocean waves

4.1 Weather parameters – high-resolution and ensemble

The supplementary headline scores for deterministic and probabilistic precipitation forecasts are shown in Figure 18. The top left panel shows the lead time at which the stable equitable error in probability space (SEEPS) skill for the high-resolution forecast for precipitation accumulated over 24 hours over the extratropics drops below 45%. The threshold has been chosen in such a way that the score measures the skill at a lead time of 3–4 days. For comparison the same score is shown for ERA5. The top right panel shows the score difference between HRES and ERA5. The bottom left panel shows the lead time at which the CRPSS for the probability forecast of precipitation accumulated over 24 hours over the extratropics drops below 10%, the bottom right panel shows the lead time where the Diagonal Skill Score (DSS) drops below 20%. The ENS thresholds have been chosen in such a way that the scores measure the skill at a lead time of about 7 days. All plots are based on verification against SYNOP observations.

The deterministic precipitation forecast has reached its highest level of skill so far. There is considerable variation in the score due to atmospheric variability, as shown by comparison with the ERA5 reference forecast (black line in Figure 18, top left panel). By taking the difference between the operational and ERA5 scores, much of this variability is removed, and the effect of model upgrades is seen more clearly (upper right panel in Figure 18). The positive effect of cycle 46r1 shows up as a substantial increase over the year 2019.

The probabilistic precipitation headline score CRPSS (lower left panel in Figure 18) shows a long-term improvement as well. However, the positive effect from cycle 46r1 is not as readily seen. The year 2019 had overall slightly higher values than 2018 but these have not yet surpassed the high point in 2015. It should be noted that in addition to the difference HRES vs ENS also the scores used (SEEPS vs CRPSS) measure different aspects of the forecast. SEEPS, as a categorical score in probability space, does not penalize errors at high precipitation values as much as the CRPSS. The DSS (lower right panel) measures, similar to SEEPS, errors in probability space and puts more weight on the discrimination aspect of the forecast, while the CRPSS is more sensitive to the reliability/calibration of the forecast. The discrimination ability of the ENS has in fact reached its highest value ever (as seen in the DSS), but the reliability has decreased somewhat so that the CRPSS has not increased as much.

ECMWF performs a routine comparison of the precipitation forecast skill of ECMWF and other centres for both the high-resolution and the ensemble forecasts using the TIGGE data archived in the Meteorological Archival and Retrieval System (MARS). Results using these same headline scores for the last 12 months show both the HRES and ENS leading with respect to the other centres (Figure 19). ECMWF’s probabilistic precipitation forecasts retain positive skill beyond day 9.

Trends in mean error (bias) and standard deviation for 2 m temperature, 2 m dewpoint, total cloud cover, and 10 m wind speed forecasts over Europe are shown in Figure 20 to Figure 23. Verification is performed against SYNOP observations. The matching of forecast and observed value uses the nearest grid-point method. A standard correction of 0.0065 K m^{-1} for the difference between model orography and station height is applied to the temperature forecasts.

For 2 m temperature (Figure 20), the reduction in error standard deviation (upper curves) which started around 2016, has continued in 2019. Biases in 2 m temperature (lower curves) have however remained very similar to previous years. For 2 m dewpoint (Figure 21), error standard deviation shows little change in 2019, but the dry bias (especially during the day) has been slightly reduced. Systematic errors in near-surface parameters have been investigated in the USURF project (‘Understanding uncertainties in surface-atmosphere exchange’), which has helped to identify the causes of some of the biases and informed ongoing and future model changes (Haiden et al., 2018; Schmederer et al., 2019). A comprehensive summary of the USURF activities, which have ended in 2020, and their main outcomes, has been published.

For total cloud cover (Figure 22) and 10 m wind speed (Figure 23) there has been little change, both in terms of error standard deviation and bias.

It is worth noting that the mean errors documented in Figure 20 to Figure 23 do not show the full range of biases on the regional scale, due to compensation effects. For example, in winter there is a positive night-time bias in 2 m temperature of several K in northern Scandinavia, while in the rest of Europe there is a negative bias of 0.5-1 K. As a result of USURF, these issues are now better understood. For example, the positive night-time bias in northern Scandinavia in winter is partly due to the use of a single-layer model of snow on the ground, and a multi-layer scheme is currently being prepared for inclusion in one of the next model cycles.

ERA5 is useful as a reference forecast for the HRES, as it allows filtering out some of the effects of atmospheric variations on scores. Figure 24 shows the evolution of skill at day 5 relative to ERA5 in the northern hemisphere extratropics for various upper-air and surface parameters. The metric used is the error standard deviation. Curves show 12-month running mean values. Improvements in near-surface variables are generally smaller than those for upper-air parameters, partly because they are verified against SYNOP, which implies a certain representativeness mismatch that is a function of model resolution. For the upper-air variables (verification against analysis), the positive effect from 46r1 is quite strong, and the largest of the last 5 years. For the near-surface variables, there is a clear signal in 2 m temperature, and slight positive effects for 10 m wind speed and total cloud cover.

The fraction of large 2 m temperature errors in the ENS has been adopted as an additional ECMWF headline score. An ENS error is considered ‘large’ in this context whenever the CRPS exceeds 5 K. Figure 25 shows that in the annual mean (red curve) this fraction has decreased from about 7% to 4.5% over the last 15 years, and that there are large seasonal variations, with values in winter more than twice as high as in summer. The beneficial effect of the resolution upgrade in 2016 is apparent, but further improvements were achieved by more recent model upgrades. The winter 2019-20 is the 6th winter in succession that shows a reduction in the number of large errors compared to the previous one.

A similar measure of the skill in predicting large 10 m wind speed errors in the ENS is shown in Figure 26. Here, a threshold of 4 m/s for the CRPS is used, to obtain similar fractions as for temperature. As for temperature, the 2016 resolution upgrade has resulted in a substantial decrease of the large error fraction. Whether the recent slight increase, driven by winter 2019-20, indicates an actual reduction in skill or is just due to atmospheric variability, needs to be investigated.

4.2 Ocean waves

The quality of the ocean wave model analysis and forecast is shown in the comparison with independent ocean buoy observations in Figure 27. While errors in 10 m wind speed have not changed too much in 2019 compared to previous years, the wave height forecasts have further improved. This is also seen in the verification against analysis (Figure 28). Improvements from cycle 46r1 are most evident in the 5-day forecasts (red curves) and, in the southern hemisphere, also in the 10-day forecast.

ECMWF has become the WMO Lead Centre for Wave Forecast Verification, and in this role, it collects forecasts from wave forecasting centres to verify them against buoy observations. An example of this comparison is shown in Figure 29 for the 3-month period March-May 2020. In the extratropics, ECMWF and Meteo-France (which uses ECMWF winds) generally lead other centres in significant wave height, while for peak period ECMWF is within the bundle of models, ranking between 3rd and 5th. In the tropics (Figure 30), ECMWF is leading in terms of peak period, and ranking 2nd for significant wave height. This difference in ranking between extratropics and tropics is partially due to different wave characteristics and partly due to the different distribution of buoys in terms of proximity to coasts between extratropics and tropics.

A comprehensive set of wave verification charts is available on the ECMWF website at

http://www.ecmwf.int/en/forecasts/charts

under ‘medium-range verification’ (select parameter ‘Ocean waves’). Verification results from the WMO Lead Centre for Wave Forecast Verification can be found at https://confluence.ecmwf.int/display/WLW/WMO+Lead+Centre+for+Wave+Forecast+Verification+LC-WFV

5 Severe weather

Supplementary headline scores for severe weather are:

- The skill of the Extreme Forecast Index (EFI) for 10 m wind speed verified using the relative operating characteristic area (Section 5.1)
- The tropical cyclone position error for the high-resolution forecast (Section 5.2)

5.1 Extreme Forecast Index (EFI)

The Extreme Forecast Index (EFI) was developed at ECMWF as a tool to provide early warnings for potentially extreme events. By comparing the ensemble distribution of a chosen weather parameter to the model’s climatological distribution, the EFI indicates occasions when there is an increased risk of an extreme event occurring. Verification of the EFI has been performed using synoptic observations over Europe from the GTS. An extreme event is judged to have occurred if the observation exceeds the 95th percentile of the observed climate for that station (calculated from a moving 15-year sample). The ability of the EFI to detect extreme events is assessed using the relative operating characteristic (ROC). The headline measure, skill of the EFI for 10 m wind speed at forecast day-4 (24-hour period 72–96 hours ahead), is shown by the blue lines in the left column of Figure 31 (top), together with results for days 1–3 and day 5. Corresponding results for 24-hour total precipitation (centre) and 2 m temperature (bottom) are shown as well. Each plot contains seasonal values, as well as the four-season running mean, of ROC area skill scores; the final point on each curve includes the spring (March–May) season 2020. For wind speed, skill has been high in 2019 compared to previous years, while for precipitation and temperature, ROC skill has reached a plateau in recent years, with some inter-annual variations.

A complementary way of verifying extremes is to use the Diagonal Elementary Skill Score DESS (Bouallegue et al., 2018), as shown in the right column of Figure 31 for the same three variables. It is based on verification in probability space and, like the ROC area, it emphasizes the discrimination aspect of the forecast. As for the EFI, the 95th quantile is used, but for wind and temperature, instantaneous rather than daily averages are used. Another difference between the two methods is that in the computation of the DESS, observation uncertainty (representativeness) has been explicitly taken into account using the method described in Bouallegue et al. (2020).

It can be seen that in terms of the DESS, forecast skill has increased more continuously in recent years than in terms of EFI ROC area. Medium-range (day 5, red curves) performance has reached a new high point for all three parameters in 2019.

5.2 Tropical cyclones

The tropical cyclone position error for the 3-day high-resolution forecast is one of the two supplementary headline scores for severe weather. The average position errors for the high-resolution medium-range forecasts of all tropical cyclones (all ocean basins) over the last ten 12-month periods are shown in Figure 32. Errors in the forecast central pressure of tropical cyclones are also shown. The comparison of HRES and ENS control (central four panels) demonstrates the benefit of higher resolution for some aspects of tropical cyclone forecasts.

Both HRES and ENS position errors at day 5 (top and bottom panels, Figure 32) have increased in the latest season. Comparison with ERA5 (grey curves) shows that this is due to variations in predictability. The HRES mean absolute error of intensity has further decreased, and the grey curve shows that this is an actual improvement also relative to ERA5.

The bottom panel of Figure 32 shows the spread and error of ensemble forecasts of tropical cyclone position. For reference, the HRES error is also shown. The forecast was generally under-dispersive before the resolution upgrade in 2010, but the spread-error relationship has improved since then. At day 3, the spread has become more underdispersive again, however for day 5 the match between spread and error is quite good.

The ensemble tropical cyclone forecast is presented on the ECMWF website as a strike probability: the probability at any location that a reported tropical cyclone will pass within 120 km during the next 240 hours. Verification of these probabilistic forecasts for the three latest 12-month periods is shown in Figure 33. Results show a small increase in reliability compared to the previous year (top panel), but still less than 2 years before. Skill is shown by the ROC and the modified ROC, the latter using the false alarm ratio (fraction of yes forecasts that turn out to be wrong) instead of the false alarm rate (ratio of false alarms to the total number of non-events) on the horizontal axis. This removes the reference to non-events in the sample and shows more clearly the reduction in false alarms in those cases where the event is forecast. For both measures, strike probability skill has increased in the most recent season but not quite reached the level of 2 years ago.

6 Monthly and seasonal forecasts

6.1 Monthly forecast verification statistics and performance

Figure 34 shows the probabilistic performance of the monthly forecast over the extratropical northern hemisphere for summer (JJA, top panels) and winter (DJF, bottom panels) seasons since September 2004 for week 2 (days 12–18, left panels) and week 3+4 (days 19–32 right panels). Curves show the ROC score for the probability that the 2 m temperature is in the upper third of the climate distribution in summer, and in the lower third of the climate distribution in winter. Thus it is a measure of the ability of the model to predict warm anomalies in summer and cold anomalies in winter. For reference, the ROC score of the persistence forecast is also shown in each plot. Forecast skill for week 2 exceeds that of persistence by about 10%, for weeks 3 to 4 (combined) by about 5%. In weeks 3 to 4 (14-day period), summer warm anomalies appear to have slightly higher predictability than winter cold anomalies, although the latter has increased in recent winters (with the exception of 2012). In 2019, week 2 forecast skill for summer warm anomalies was somewhat lower than in 2018, however skill above persistence was comparable to 2018, also for week 2 cold anomalies. Summer week 3+4 forecast skill and persistence were near the upper end of values seen so far. Week 3+4 skill for winter cold anomalies in 2019 was high, but only marginally higher than persistence.

Because of the low signal-to-noise ratio of real-time forecast verification in the extended range (Figure 34), re-forecasts are a useful additional resource for documenting trends in skill. Figure 35 shows the skill of the ENS in predicting 2 m temperature anomalies in week 3 in the northern extratropics. This is an additional headline score of ECMWF which was recommended by the TAC Subgroup on Verification. Verification against both SYNOP and ERA-Interim analyses shows that there has been a substantial increase in skill from 2005-2012, and little change (against analysis), and a slight decrease (against observations) thereafter. However, a marked increase is seen in 2020, which is mainly due to ERA5 replacing ERA-Interim as initial condition for the reforecasts. Due to this change, the reforecast skill has in a way ‘caught up’ again and has become more representative of real-time forecast skill. Note also that the verification is based on a sliding 20-year period and is therefore less sensitive to changes from year to year than the real-time forecast evaluation, but some sensitivity remains, e.g. due to major El Niño events falling within, or dropping out of, the sliding period.

An evaluation of forecast skill from the medium to the extended range in terms of large-scale Euro-Atlantic regimes and their effect on severe cold anomalies in Europe has been given by Ferranti et al. (2018).

Comprehensive verification for the monthly forecasts is available on the ECMWF website at:

http://www.ecmwf.int/en/forecasts/charts

6.2 Seasonal forecast performance

6.2.1 Seasonal forecast performance for the global domain

The current version SEAS5 of the seasonal component of the IFS (implemented in November 2017) includes updated versions of the atmospheric (IFS) and interactive ocean (NEMO) models and adds the interactive sea ice model LIM2. While re-forecasts span 36 years (from 1981 to 2016), the re-forecast period used to calibrate the forecasts when creating products uses the more recent period 1993 to 2016. Compared to the previous version, SEAS5 shows an improvement in SST drift, especially in the tropical Pacific, and improvements in the prediction skill of Arctic sea ice.

A set of verification statistics based on re-forecast integrations from SEAS5 has been produced and is presented alongside the forecast products on the ECMWF website at

www.ecmwf.int/en/forecasts/charts

by choosing ‘Verification’ under the header ‘Long Range’. A comprehensive user guide for SEAS5 is provided at:

https://www.ecmwf.int/sites/default/files/medialibrary/2017-10/System5_guide.pdf

6.2.2 The 2019–2020 El Niño forecasts

The summer of 2019 was characterized by a return from weakly positive SST anomalies to neutral conditions in the eastern tropical Pacific. While this scenario was among those given by the ensemble forecasts in May 2019 (Figure 36, top row), the spread both in SEAS5 and C3S was very large such that no clear guidance could be derived from the forecast. Forecasts for subsequent seasons had less spread, and correctly indicated an evolution toward small positive SST anomalies. The second return to neutral conditions in spring 2020 (and the change to even slightly negative SST anomalies) was indicated qualitatively, but the timing was not captured well. Forecasts at first predicted the change too early and subsequently too late. Comparison of SEAS5 and C3S shows that the multi-model ensemble, due to its larger spread, better covers the observed evolution. Comparing the forecasts of Nov 2019 and Feb 2020 (Figure 36, 3rd and 4th rows) we can see that C3S does not indiscriminately produce more spread, and that the spread difference between the two could be used as additional guidance.

6.2.3 Tropical storm predictions from the seasonal forecasts

The 2019 Atlantic hurricane season had a total of 18 named storms including 6 hurricanes and 3 major hurricanes. It was the fourth consecutive above-average and damaging season, with an accumulated cyclone energy index (ACE) of about 130% of the 1993–2015 climate average (Figure 37). Seasonal tropical storm predictions from SEAS5 indicated a below average level of activity over the Atlantic (ACE of about 60% (+/- 30%) of the 1993–2015 climate average). Similarly, the number of tropical storms (18) which formed in 2019 was above average (13) whereas the forecast predicted 8.5 (with a range from 5.5 to 11) tropical storms in the Atlantic (Figure 38). Subsequent forecasts issued in July and August predicted an average season. This poor seasonal forecast can partly be related to the overestimation of the 2019 El-Niño event as well as to the failure of the model to represent decadal changes of tropical cyclone activity including the increased tropical cyclone activity over the Atlantic since 2016.

Figure 38 also shows that SEAS5 predicted above average activity over the eastern North Pacific and western North Pacific (ACE of about 110% of the 1993–2015 climate average). The 2019 Pacific typhoon season was indeed an above-average season producing 29 storms, 17 typhoons, and 4 super typhoons, with an ACE about 10% above average, as predicted by SEAS5. The eastern North Pacific hurricane season was also an above average season with 17 named storms from July to December (1993-2017 climate average is 12 tropical storms) while SEAS5 predicted 15.

6.2.4 Extratropical seasonal forecasts

Because of the lack of a strong El Niño or La Niña signal, low seasonal predictive skill would have been expected for 2019. However, a very strong positive phase of the Indian Ocean Dipole (IOD) peaking towards the end of 2019 became the main tropical driver of global long-range forecast skill. As a result, 2 m temperature anomaly patterns in boreal winter (DJF 2019–20) were reasonably well predicted over large parts of the globe, especially over ocean areas, including the North Atlantic (Figure 39). In mid- and high-latitude regions of the American and Eurasian continents, however, forecast skill was lower.

The extreme positive anomaly over Siberia (exceeding 1.5 standard deviations in some areas) was hinted at but not captured in magnitude, and the cold anomaly in Alaska and northern Canada was missed.

In spring 2020, both the IOD as well as temperature anomalies in the tropical Pacific returned to close-to-neutral values, leaving the 2020 boreal summer without two strong drivers on seasonal timescales. The seasonal forecast captured the weak cold anomaly in the tropical eastern Pacific (El Niño region), and the warm anomaly over the Indian Ocean and, in part, the strong warm anomalies around Antarctica (Figure 40). However, in the Northern Hemisphere, and especially over the continents, there is little resemblance between forecast and analysis. This includes Europe, where a cold anomaly in the Mediterranean area, and higher than normal temperatures in most of Scandinavia (forming the western extension of the strong Siberian warm anomaly) were missed in the forecast.

Since the ensemble mean carries only part of the information provided by an ensemble, we also look at the forecast distribution in the form of quantile (climagram) plots. Climagrams for Northern and Southern Europe for winter 2019-20 and summer 2020 are shown in Figure 41. Red squares indicate observed monthly anomalies. The November 2019 forecast for winter season 2019-20 gave a good indication of the warm anomalies observed both in Northern and Southern Europe. For example, the forecast gave a high probability for a very warm January 2020 in Northern Europe, as observed. The magnitude of the anomaly was slightly higher than the 95th quantile of the forecast. The May 2020 forecast for summer 2020 was less skillful, which is expected for summer seasons in general. Whereas in winter, the sign of the forecast anomaly was predicted correctly most of the time, in summer there were more discrepancies such as a cold June in Southern Europe and and cold July in Northern Europe. In both seasons, observations fall within the ensemble distribution with few exceptions.

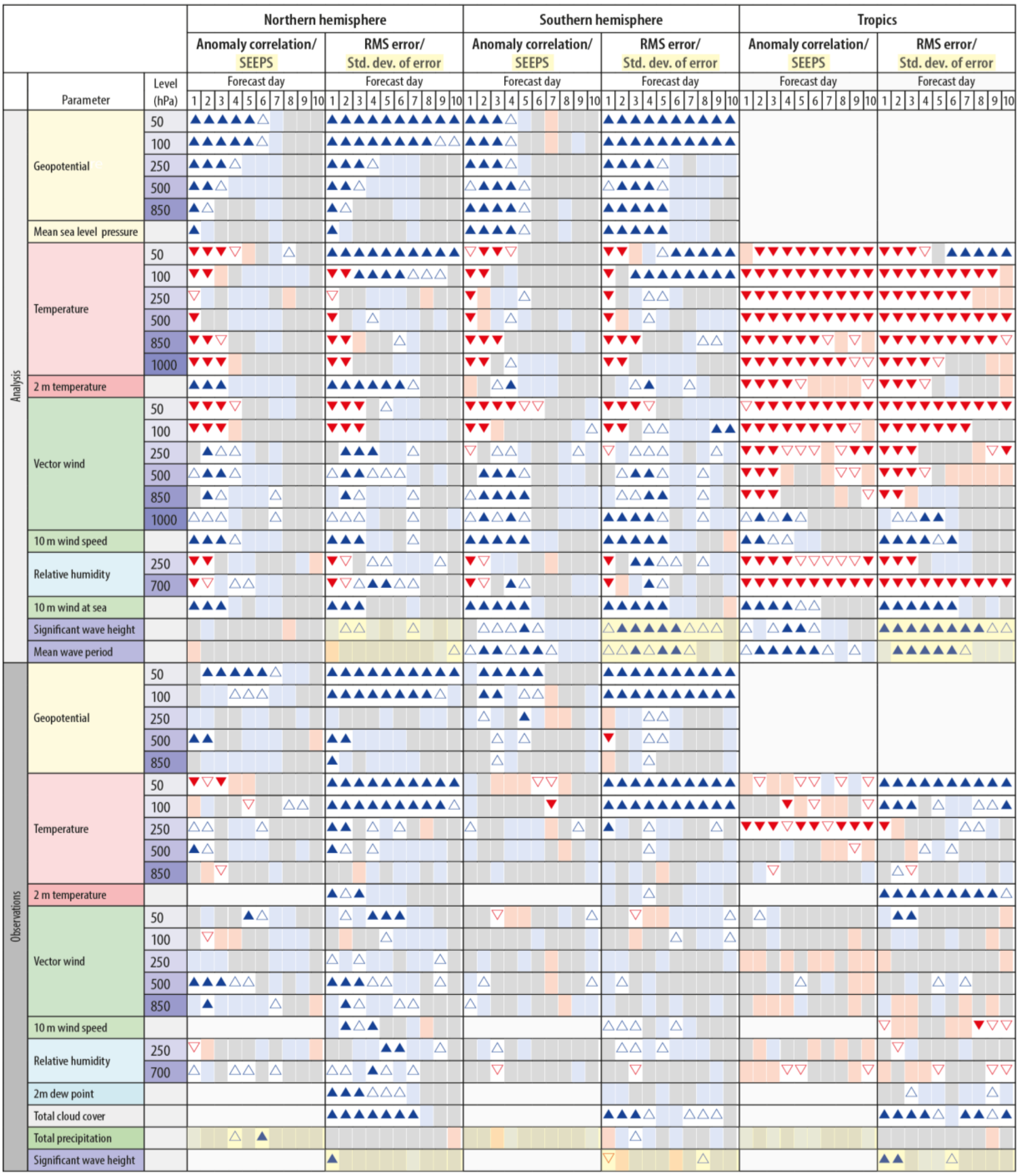

Symbol legend: for a given forecast step...

▲ 47r1 better than 46r1 statistically significant with 99.7% confidence

△ 47r1 better than 46r1 statistically significant with 95% confidence

🟦 47r1 better than 46r1 statistically significant with 68% confidence

⬜ no significant difference between 46r1 and 47r1

🟧 47r1 worse than 46r1 statistically significant with 68% confidence

▽ 47r1 worse than 46r1 statistically significant with 95% confidence

▼ 47r1 worse than 46r1 statistically significant with 99.7% confidence

Figure 1: Summary score card for IFS Cycle 47r1. Score card for HRES cycle 47r1 versus cycle 46r1 verified by the respective analyses and observations at 00 and 12 UTC for 780 forecast runs in the period December 2018 to June 2020. Yellow colouring indicates that symbols refer to the second score indicated at the top of the column.

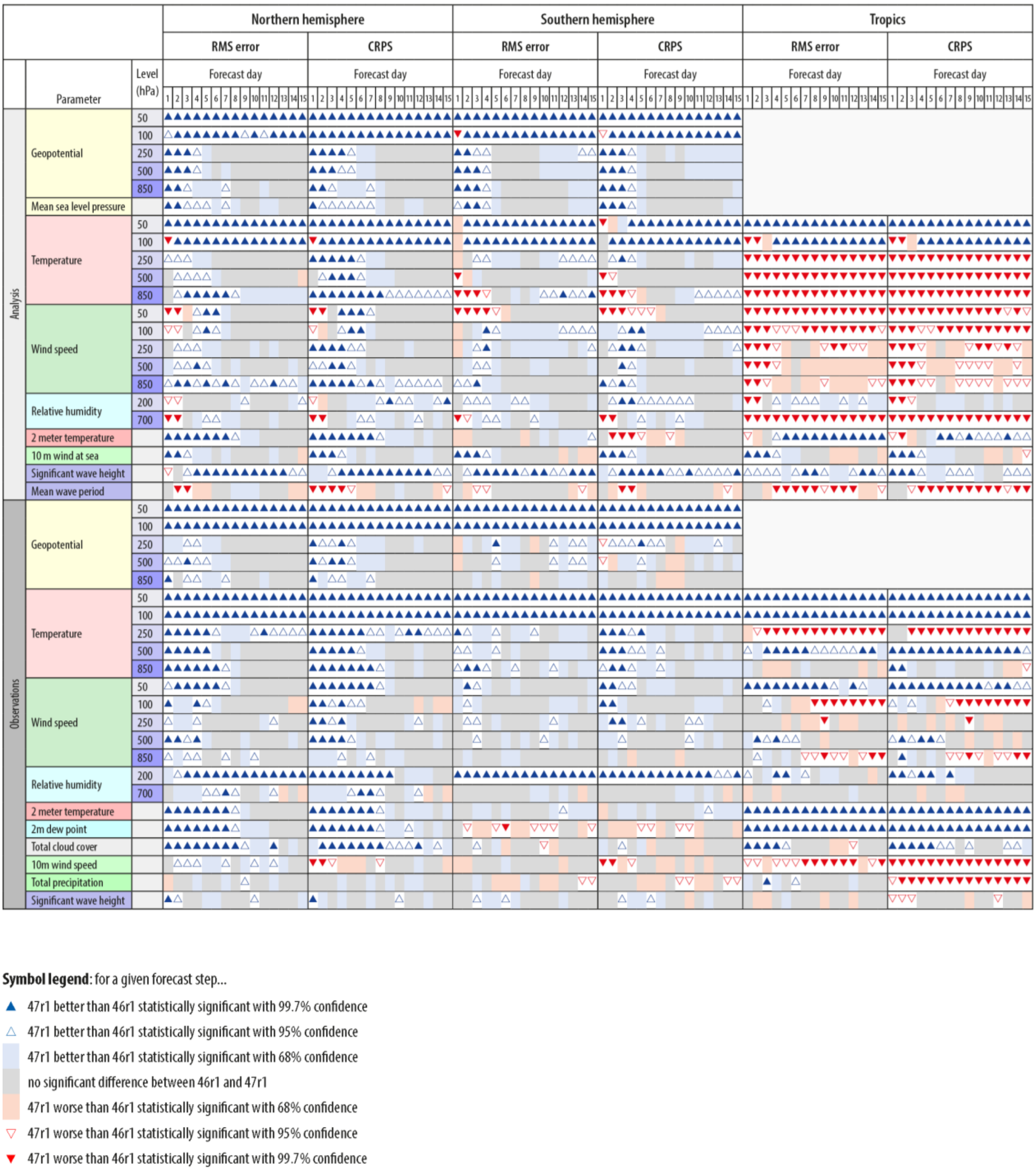

Symbol legend: for a given forecast step...

- ▲ 47r1 better than 46r1 statistically significant with 99.7% confidence
- △ 47r1 better than 46r1 statistically significant with 95% confidence
- ▨ 47r1 better than 46r1 statistically significant with 68% confidence
- ▨ no significant difference between 46r1 and 47r1
- ▨ 47r1 worse than 46r1 statistically significant with 68% confidence
- ▽ 47r1 worse than 46r1 statistically significant with 95% confidence
- ▼ 47r1 worse than 46r1 statistically significant with 99.7% confidence

Figure 2: Summary ENS score card for IFS Cycle 47r1. Score card for ENS cycle 47r1 versus cycle 46r1 verified by the respective analyses and observations at 00 UTC for 495 ENS forecast runs in the period December 2018 to June 2020.

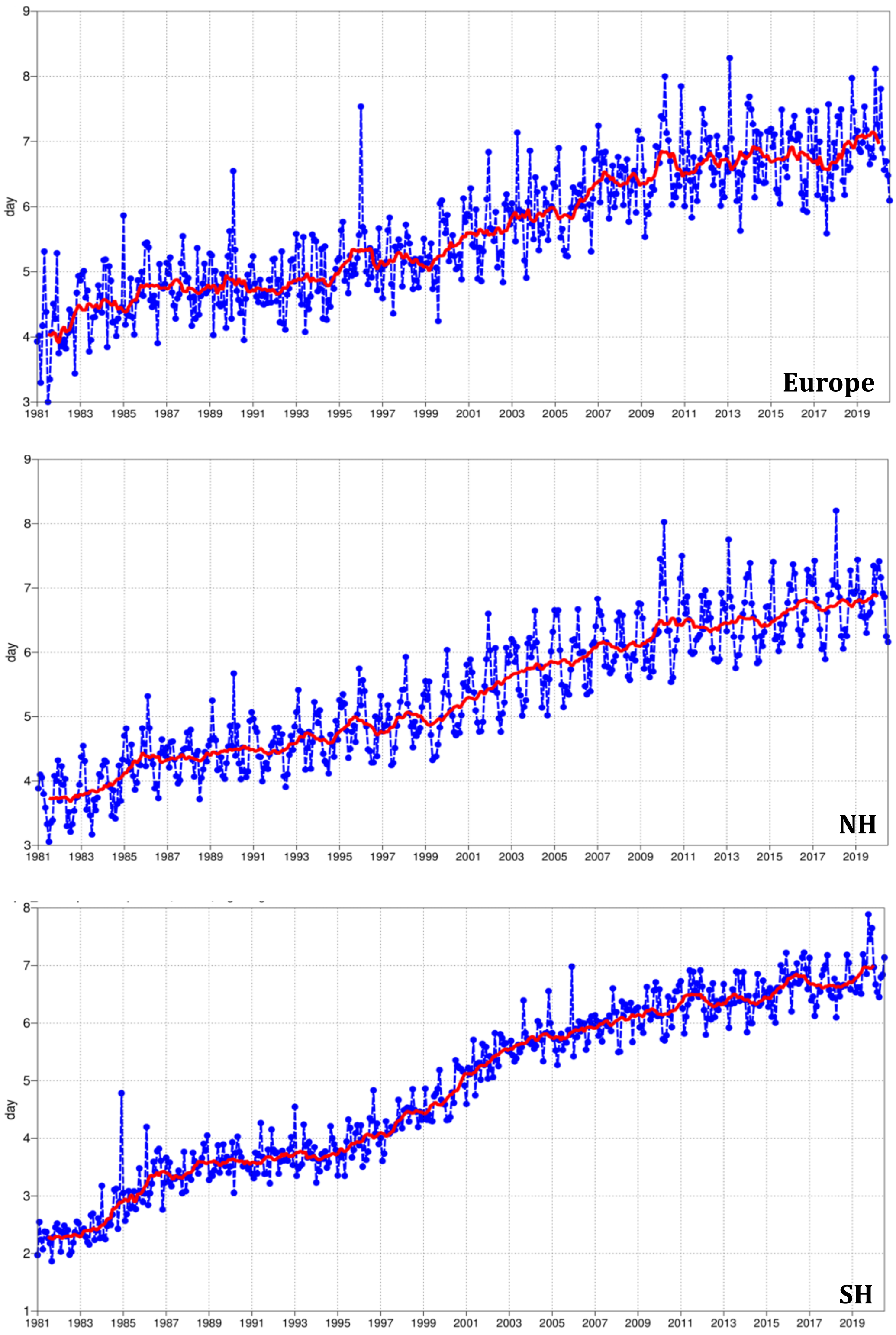

Figure 3: Primary headline score for the high-resolution forecasts. Evolution with time of the 500 hPa geopotential height forecast performance – each point on the curves is the forecast range at which the monthly mean (blue lines) or 12-month mean centred on that month (red line) of the forecast anomaly correlation (ACC) with the verifying analysis falls below 80% for Europe (top), northern hemisphere extratropics (centre) and southern hemisphere extratropics (bottom).

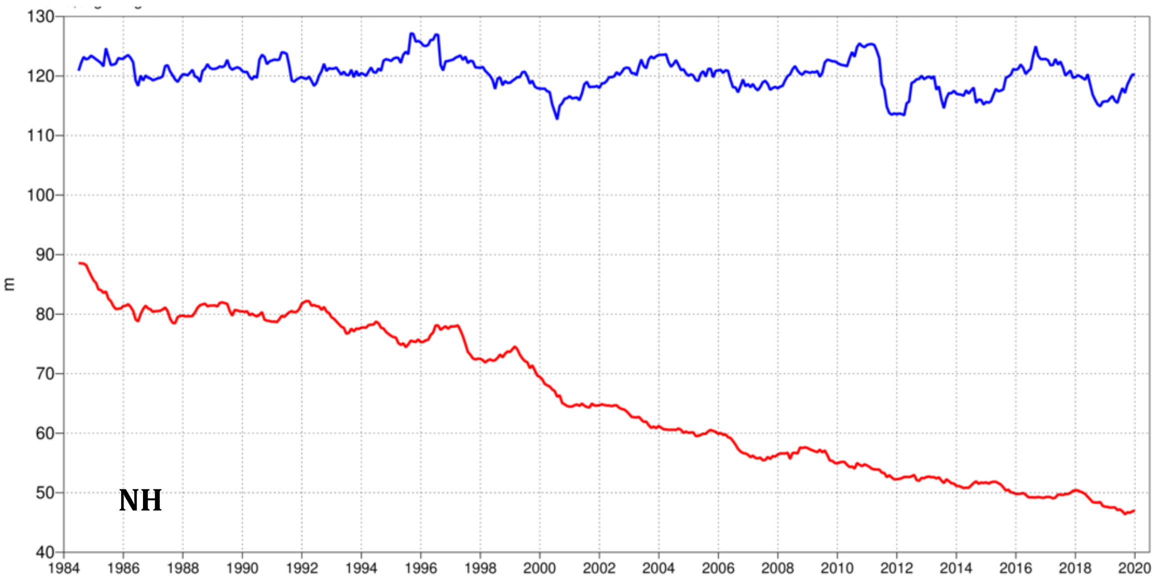

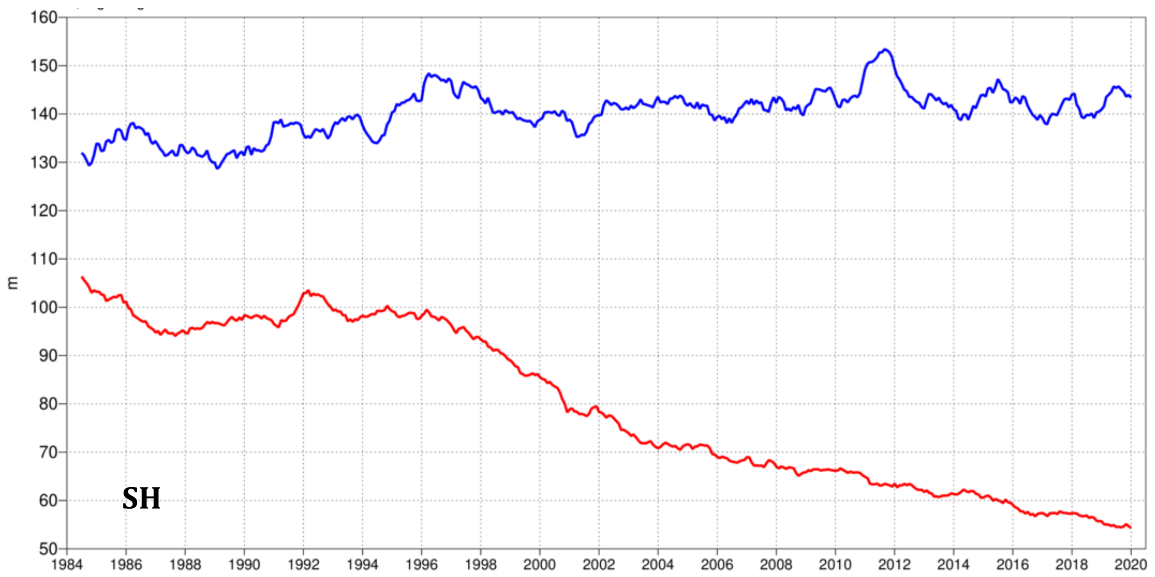

Figure 4: Root mean square (RMS) error of forecasts of 500 hPa geopotential height (m) at day 6 (red), verified against analysis. For comparison, a reference forecast made by persisting the analysis over 6 days is shown (blue). Plotted values are 12-month moving averages; the last point on the curves is for the 12-month period August 2019–July 2020. Results are shown for the northern extra-tropics (top), and the southern extra-tropics (bottom).

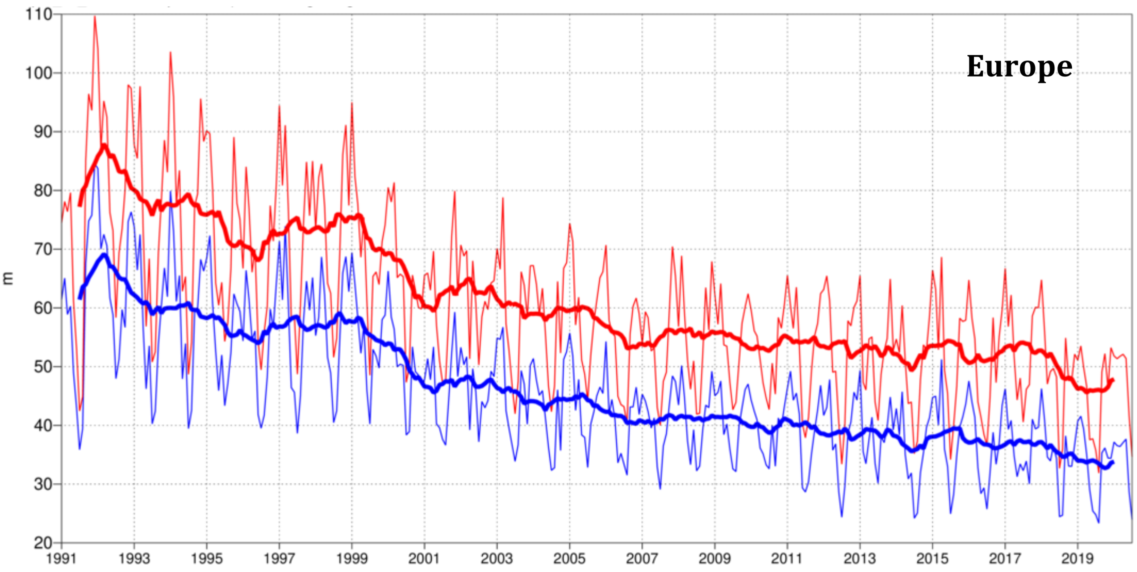

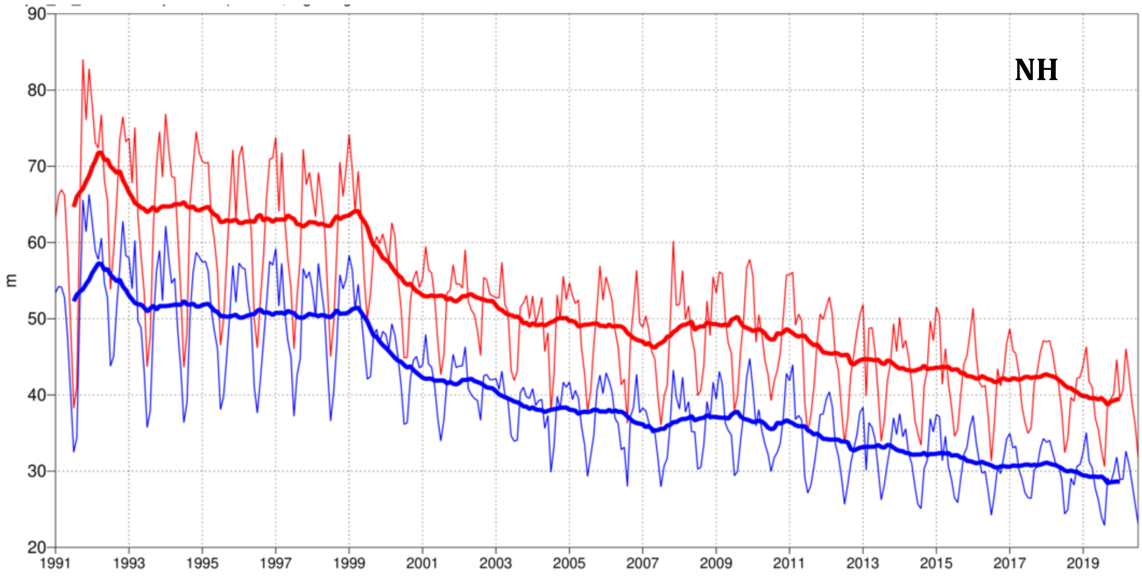

Figure 5**:** Inconsistency of the 500 hPa height forecasts over Europe (top) and northern extratropics (bottom). Curves show the monthly average RMS difference between forecasts for the same verification time but initialised 24 h apart, for 96–120 h (blue) and 120–144 h (red). 12-month moving average scores are also shown (in bold).

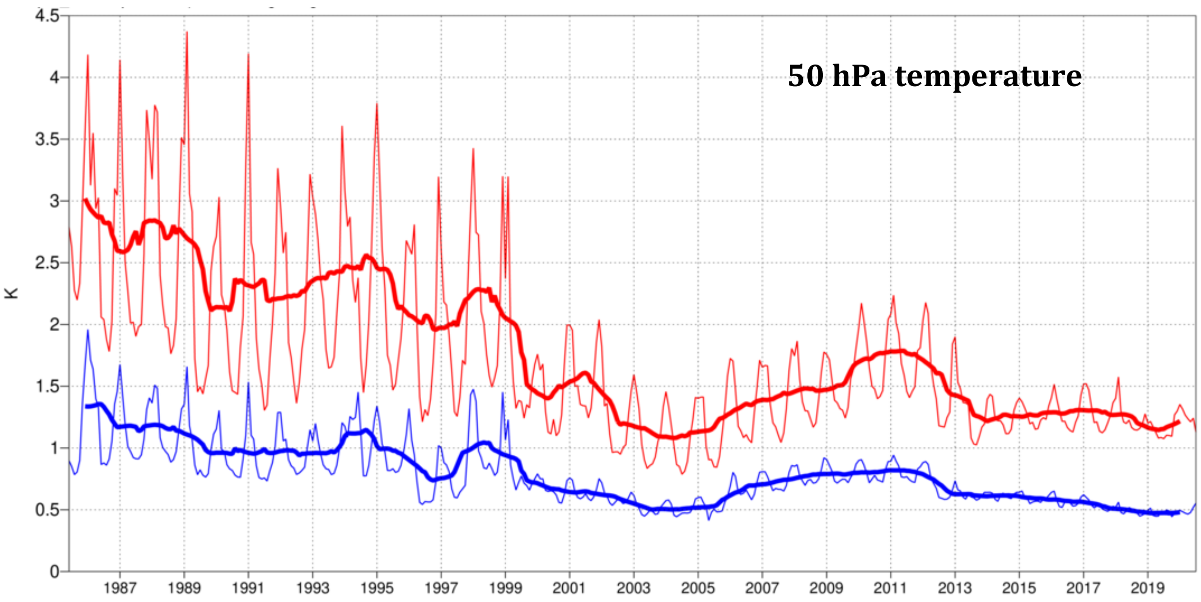

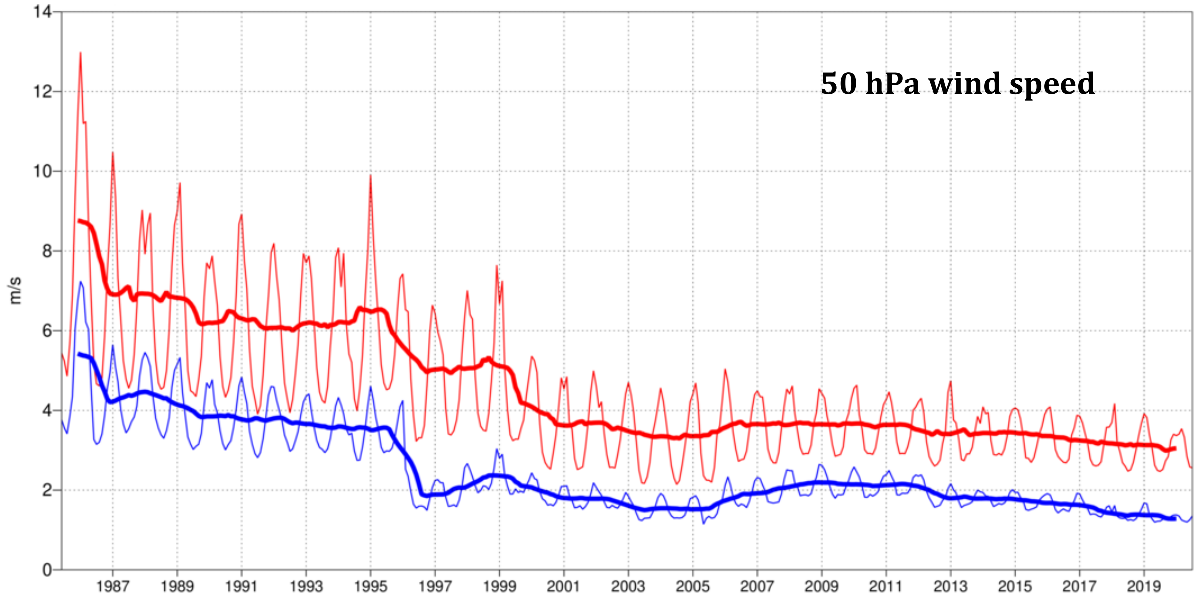

Figure 6**:** Model scores for temperature (top) and wind (bottom) in the northern extratropical stratosphere. Curves show the monthly average RMS temperature and vector wind error at 50 hPa for one-day (blue) and five-day (red) forecasts, verified against analysis. 12-month moving average scores are also shown (in bold).

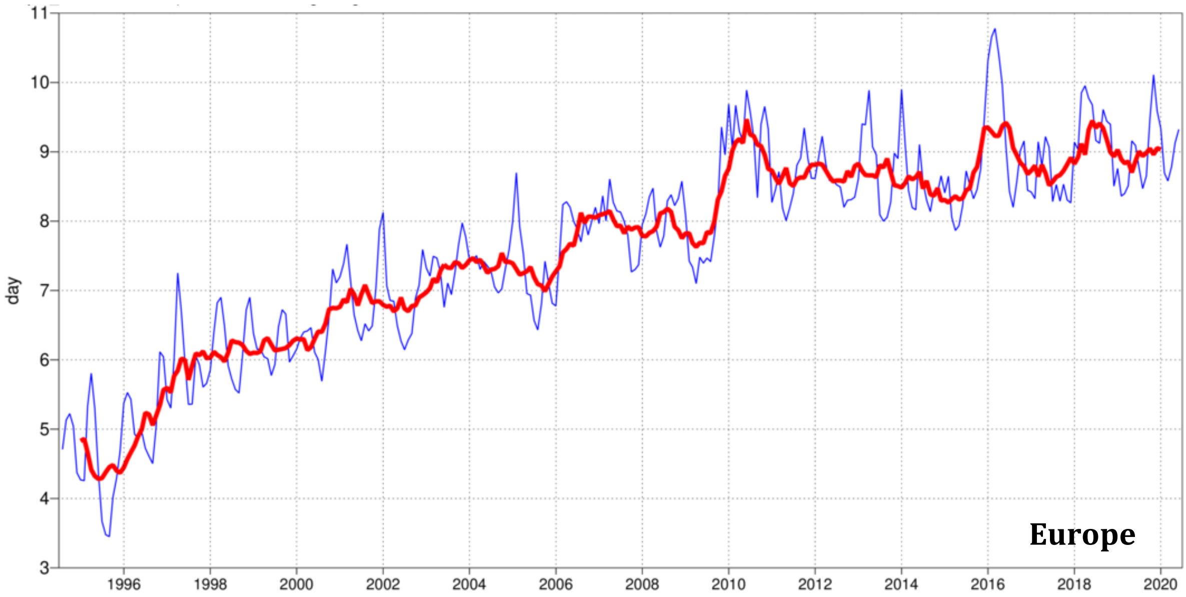

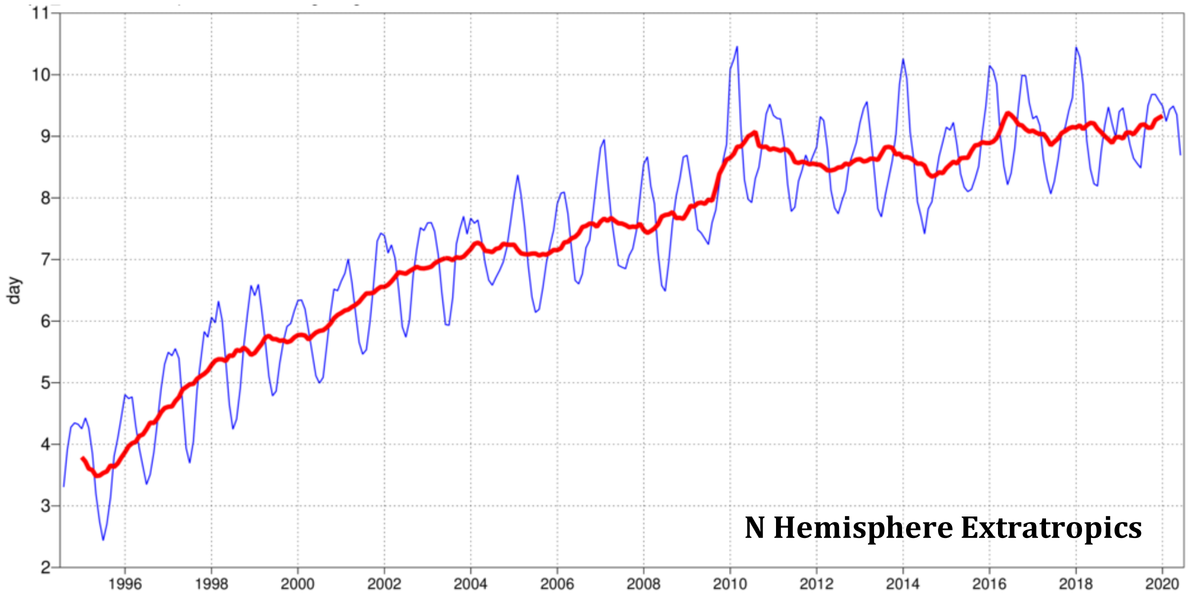

Figure 7**:** Primary headline score for the ensemble probabilistic forecasts. Evolution with time of 850 hPa temperature ensemble forecast performance, verified against analysis. Each point on the curves is the forecast range at which the 3-month mean (blue lines) or 12-month mean centred on that month (red line) of the continuous ranked probability skill score (CPRSS) falls below 25% for Europe (top), northern hemisphere extratropics (bottom).

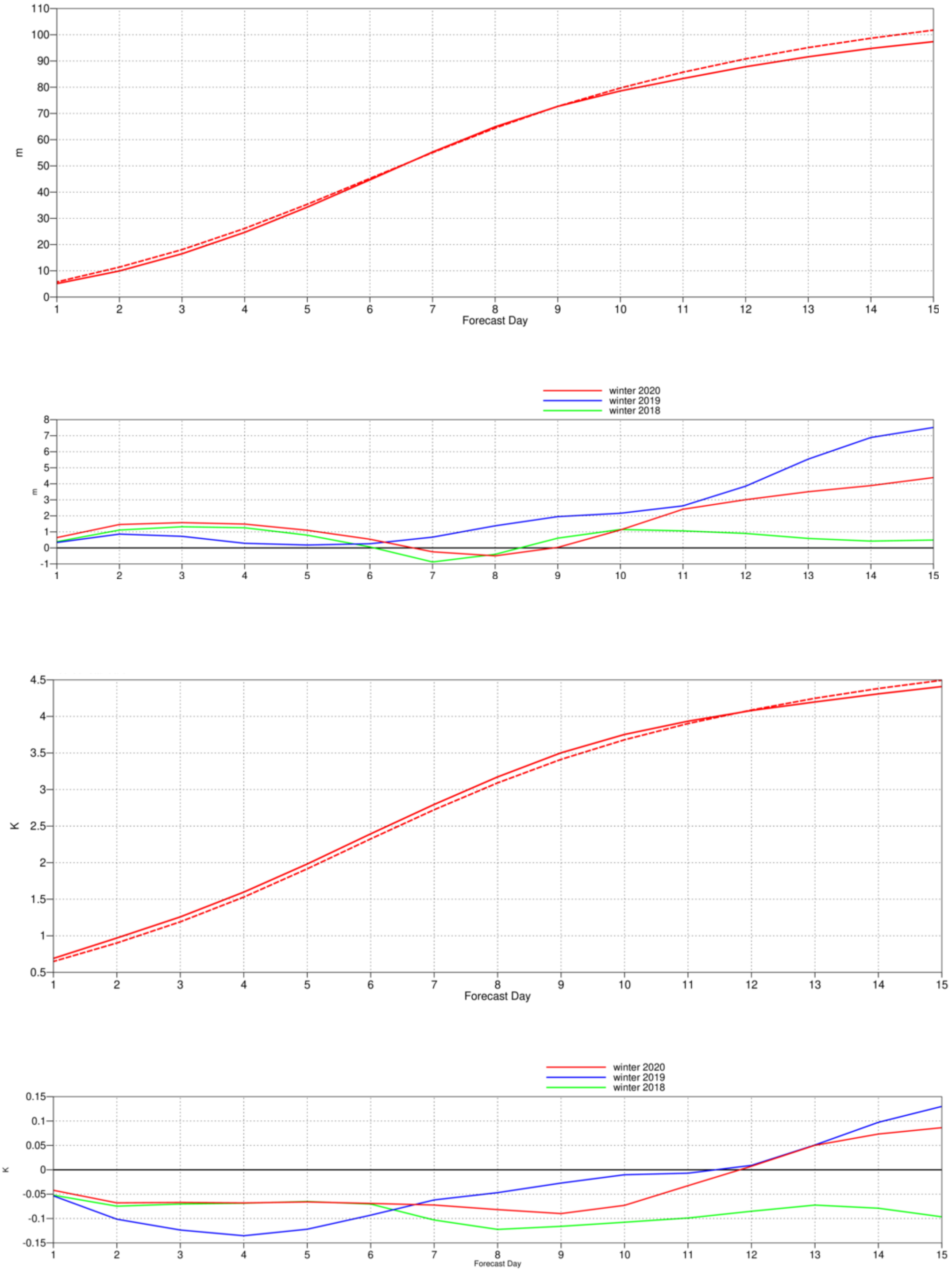

Figure 8**:** Ensemble spread (standard deviation, dashed lines) and RMS error of ensemble-mean (solid lines) for winter 2019–2020 (upper figure in each panel), and differences of ensemble spread and RMS error of ensemble mean for last three winter seasons (lower figure in each panel, negative values indicate spread is too small); verification is against analysis, plots are for 500 hPa geopotential (top) and 850 hPa temperature (bottom) over the extratropical northern hemisphere for forecast days 1 to 15.

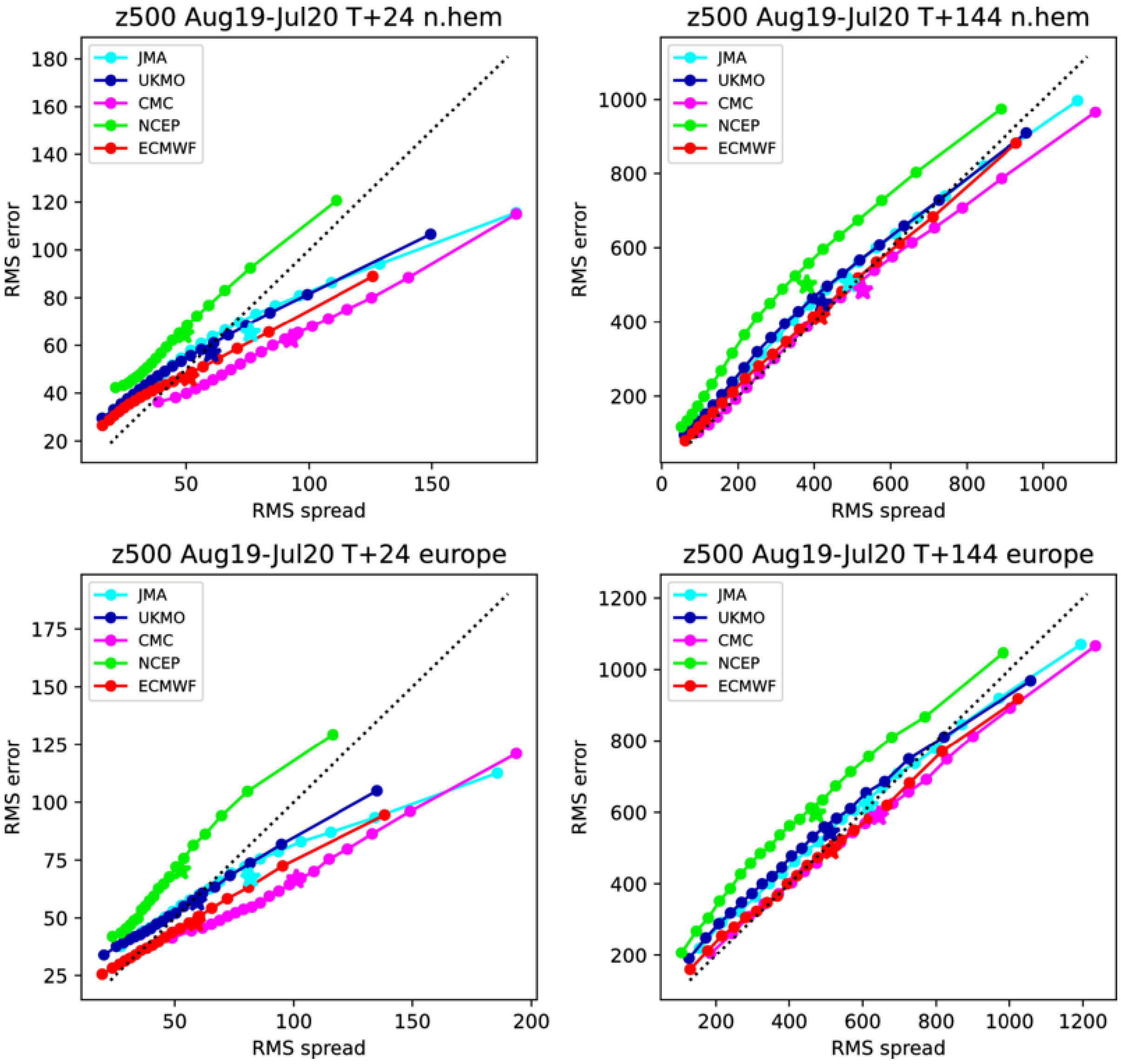

Figure 9**:** Ensemble spread reliability of different global models for 500 hPa geopotential for the period August 2019–July 2020 in the northern hemisphere extra-tropics (top) and in Europe (bottom) for day 1 (left) and day 6 (right), verified against analysis. Circles show error for different values of spread, stars show average error-spread relationship. Due to random outages in the data supply, NCEP curves are based on a reduced data set (70%).

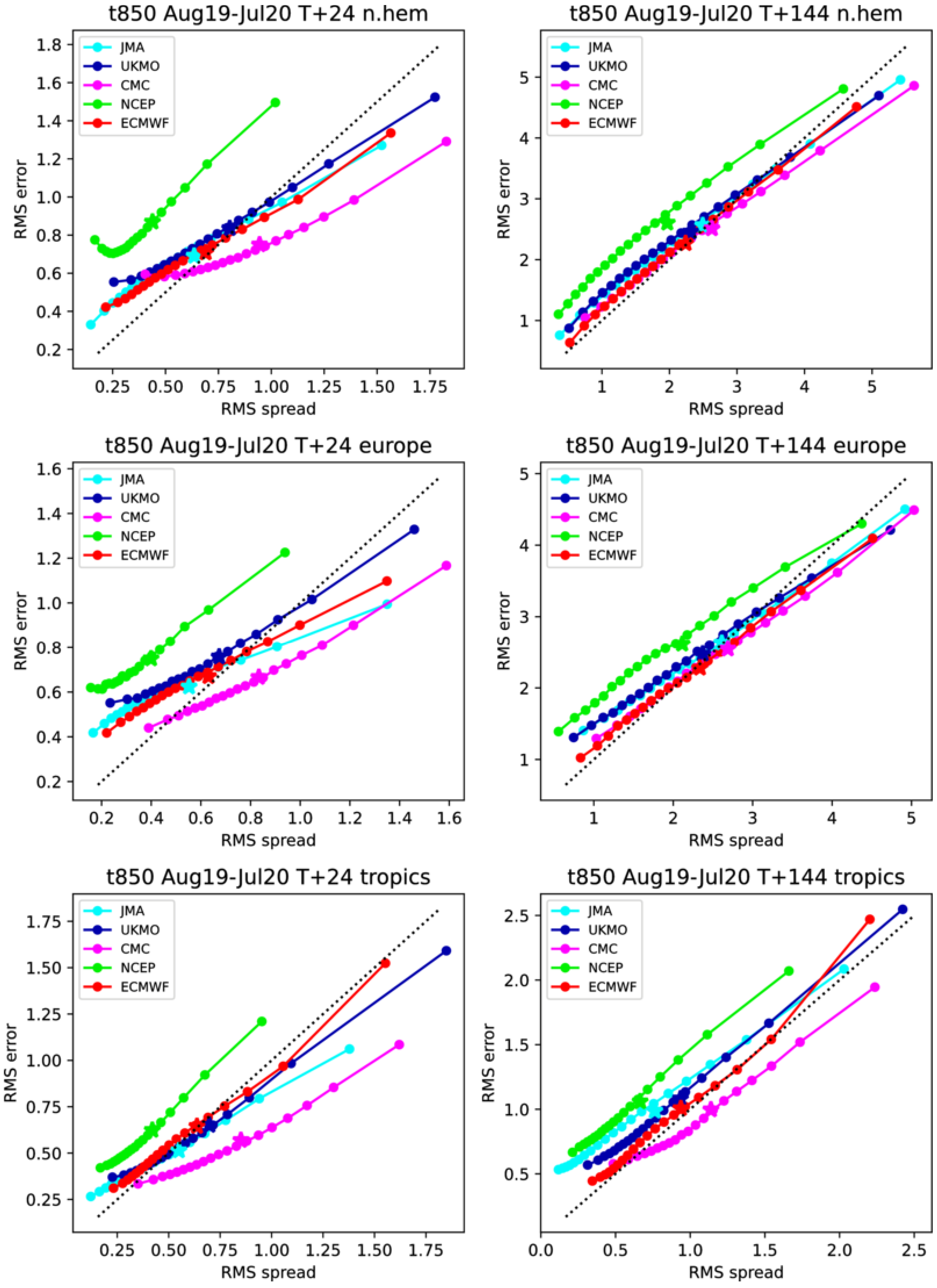

Figure 10: As Figure 9 for 850 hPa temperature.

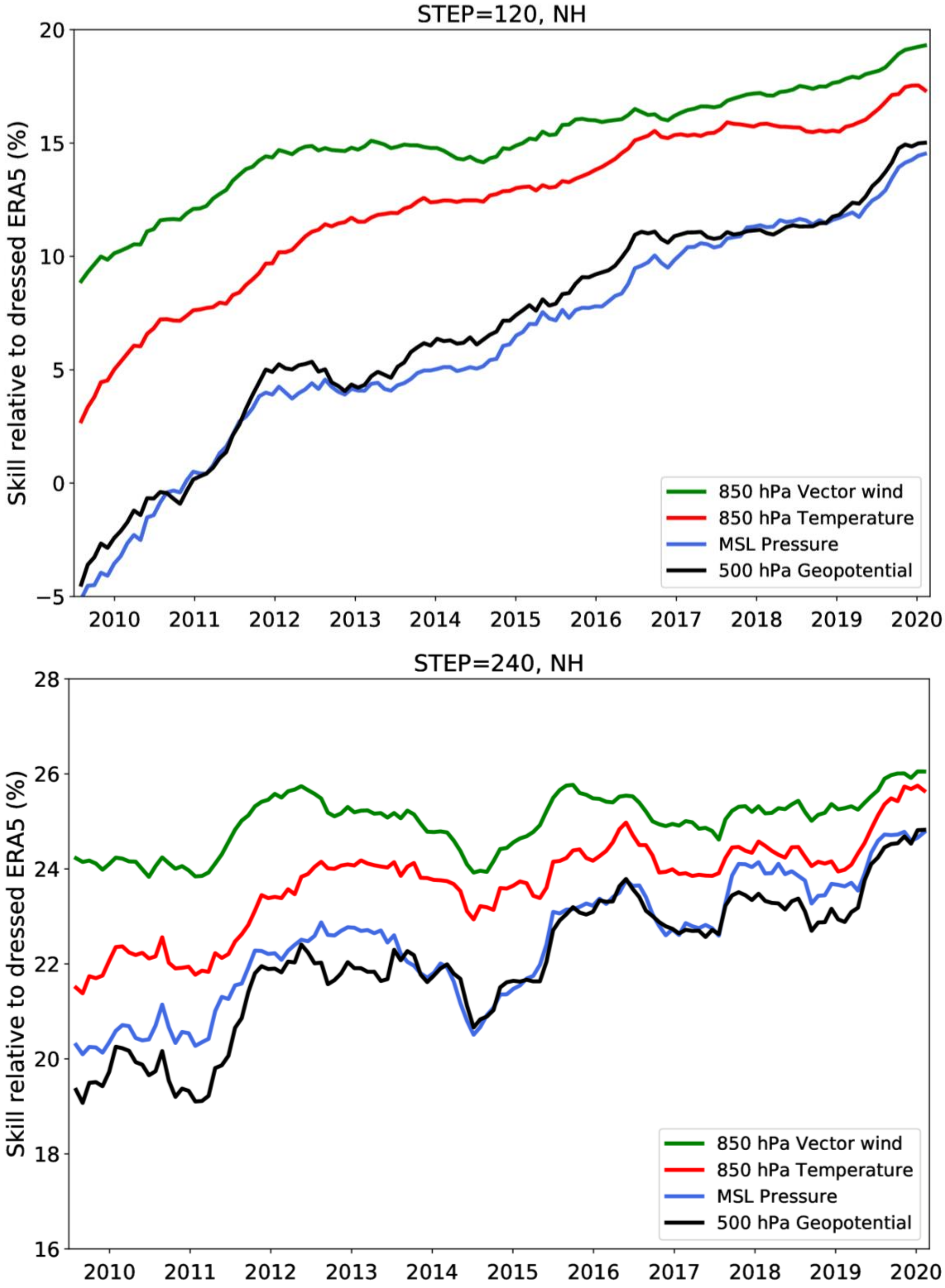

Figure 11: Skill of the ENS at day 5 (top) and day 10 (bottom) for upper-air parameters in the northern extra-tropics, relative to a Gaussian-dressed ERA5 forecast. Values are running 12-month averages, and verification is performed against own analysis.

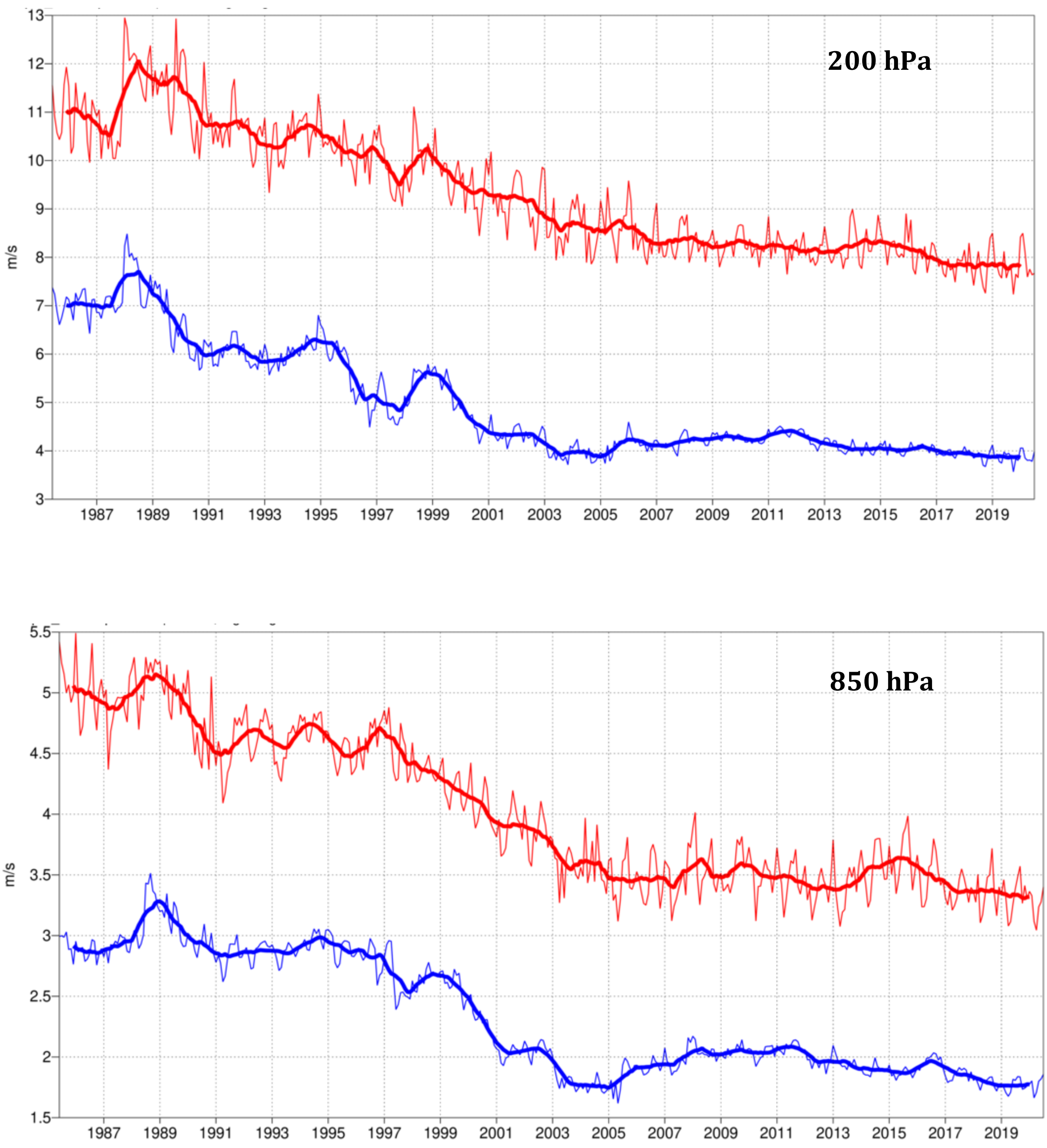

Figure 12**:** Forecast performance in the tropics. Curves show the monthly average RMS vector wind errors at 200 hPa (top) and 850 hPa (bottom) for one-day (blue) and five-day (red) forecasts, verified against analysis. 12-month moving average scores are also shown (in bold).

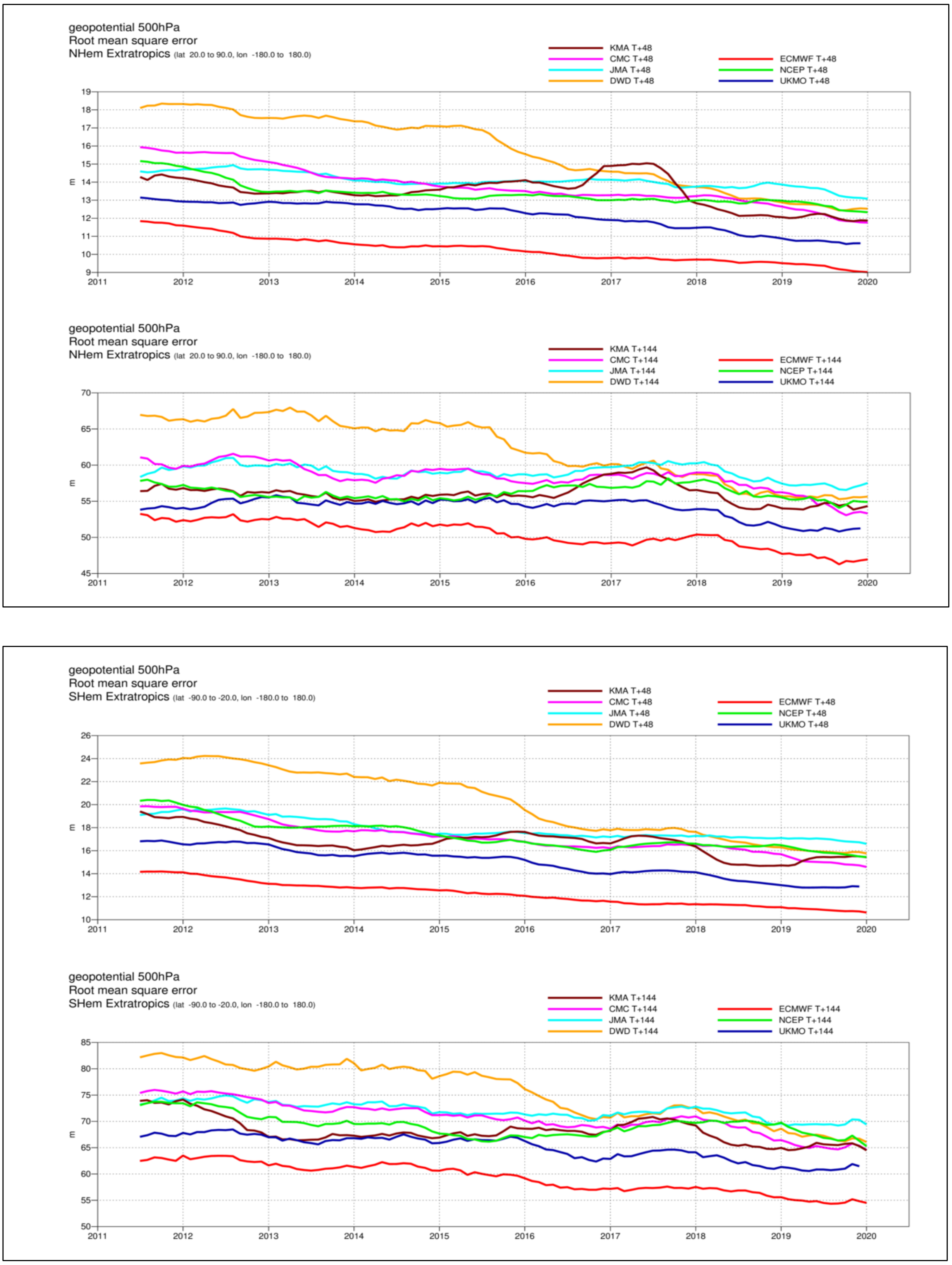

Figure 13: WMO-exchanged scores from global forecast centres. RMS error of 500 hPa geopotential height over northern (top box) and southern (bottom box) extratropics. In each box the upper plot shows the two-day forecast error and the lower plot shows the six-day forecast error of model runs initiated at 12 UTC. Each model is verified against its own analysis. JMA = Japan Meteorological Agency, CMC = Canadian Meteorological Centre, UKMO = the UK Met Office, KMA = Korea Meteorological Administration, NCEP = U.S. National Centers for Environmental Prediction, DWD = Deutscher Wetterdienst.

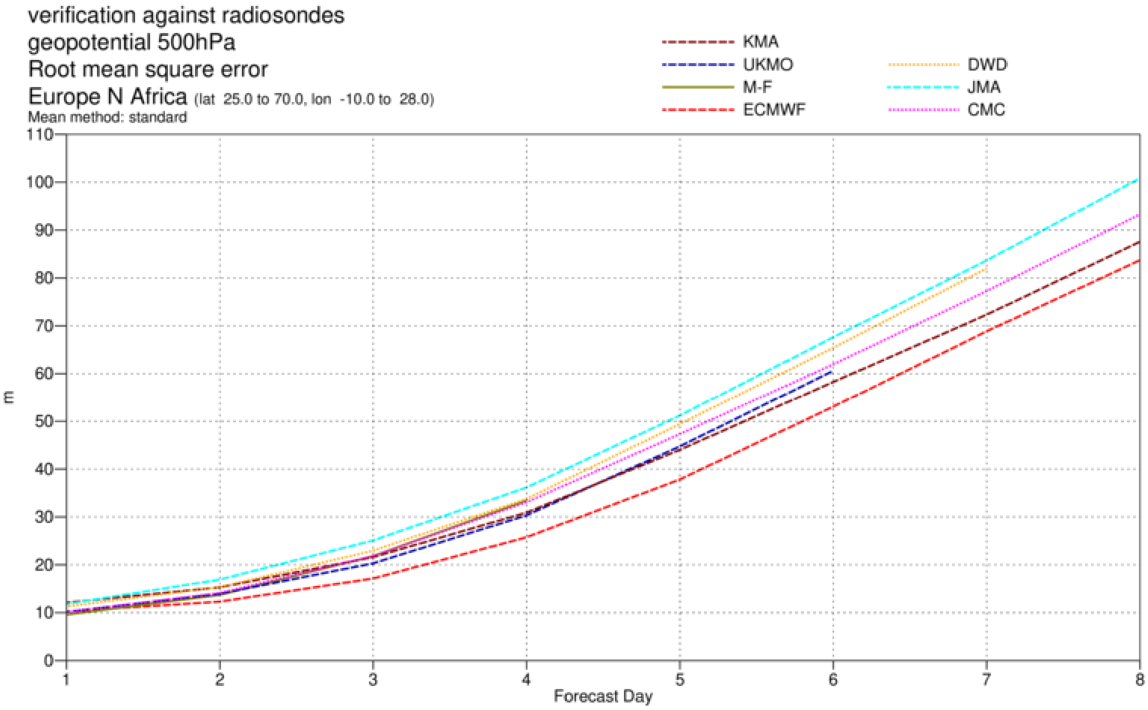

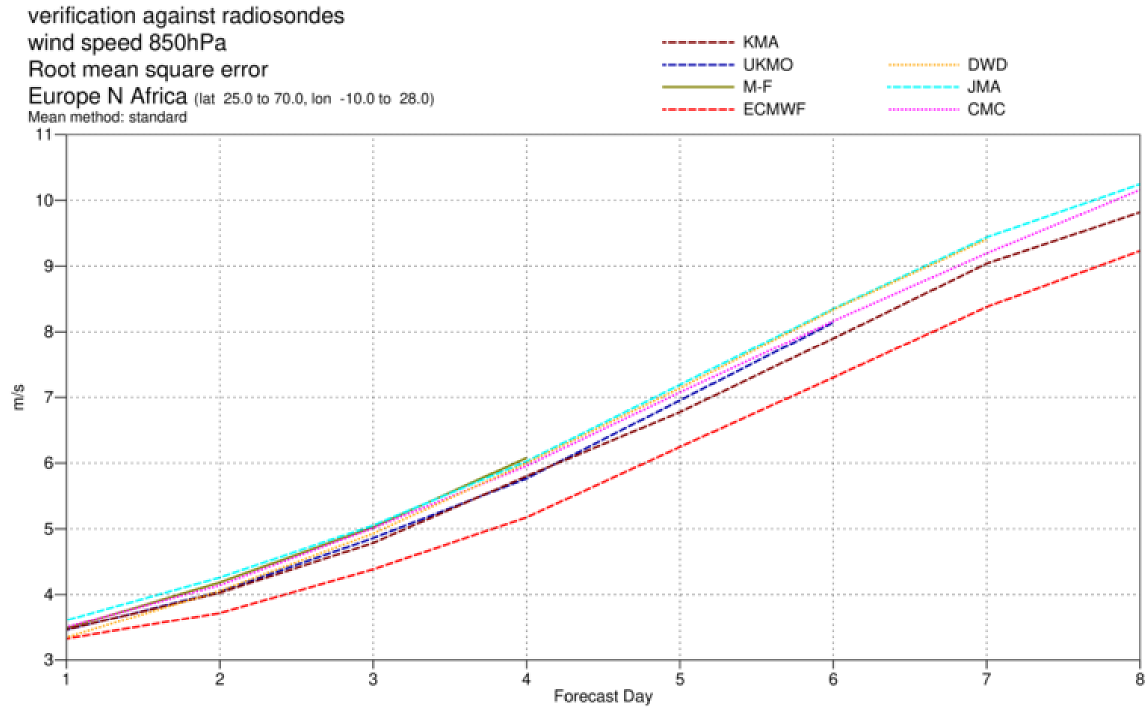

Figure 14**:** WMO-exchanged scores for verification against radiosondes: 500 hPa height (top) and 850 hPa wind (bottom) RMS error over Europe (annual mean August 2019–July 2020) of forecast runs initiated at 12 UTC.

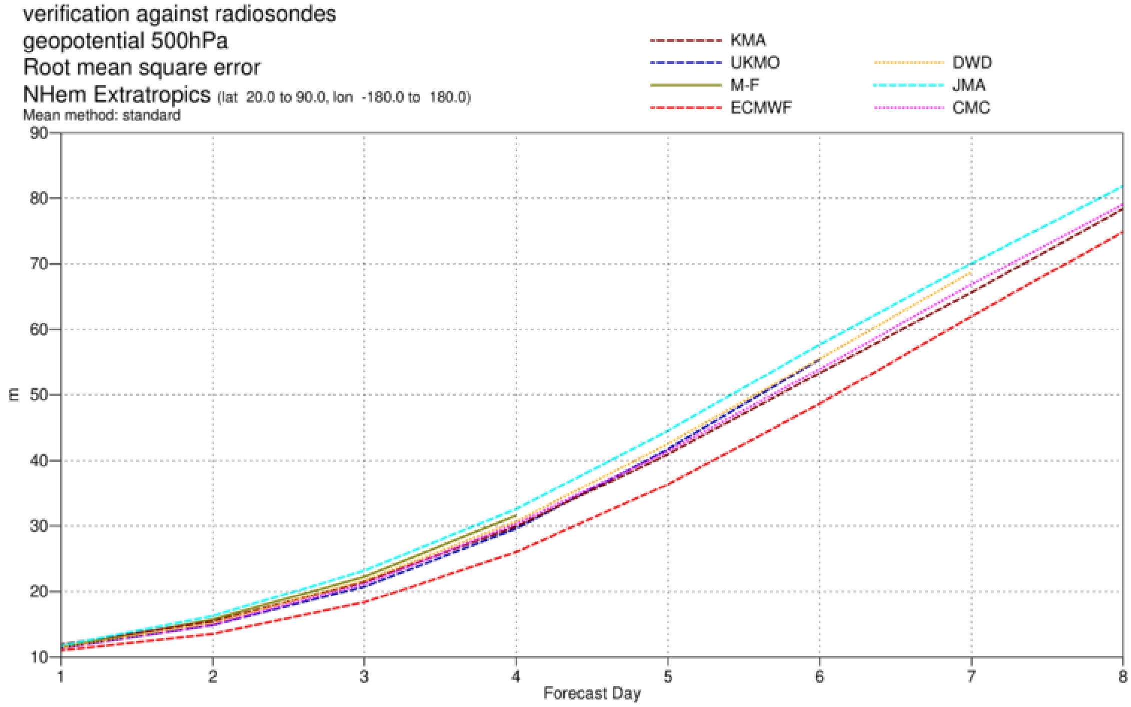

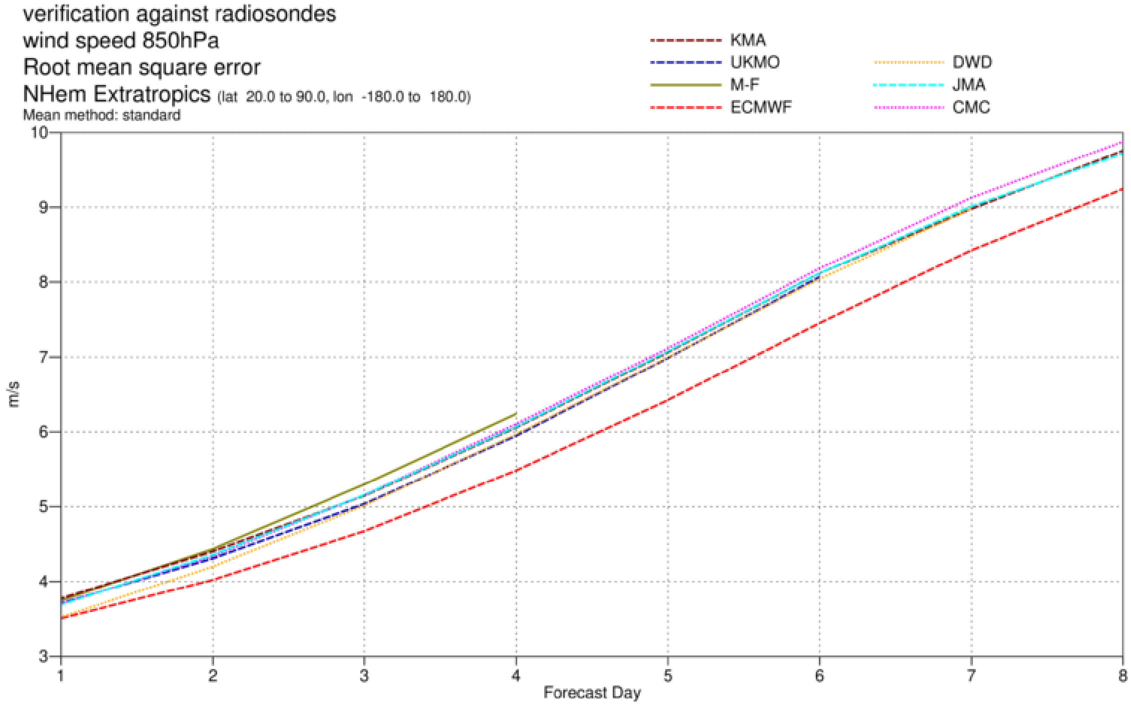

Figure 15**:** As Figure 14 for the northern hemisphere extratropics.

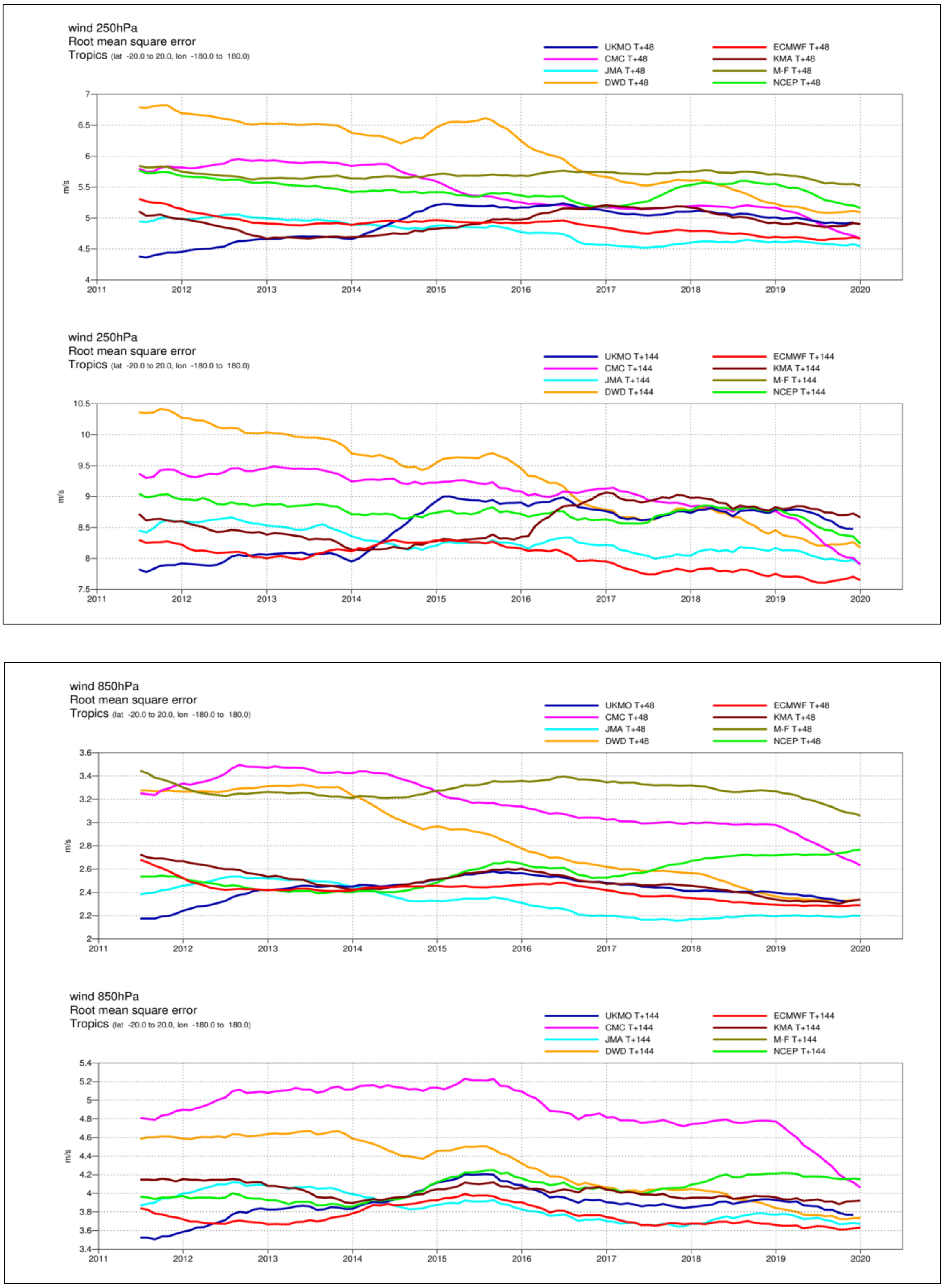

Figure 16**:** WMO-exchanged scores from global forecast centres. RMS vector wind error over tropics at 250 hPa (top box) and 850 hPa (bottom box). In each box the upper plot shows the two-day forecast error and the lower plot shows the six-day forecast error of model runs initiated at 12 UTC. Each model is verified against its own analysis.

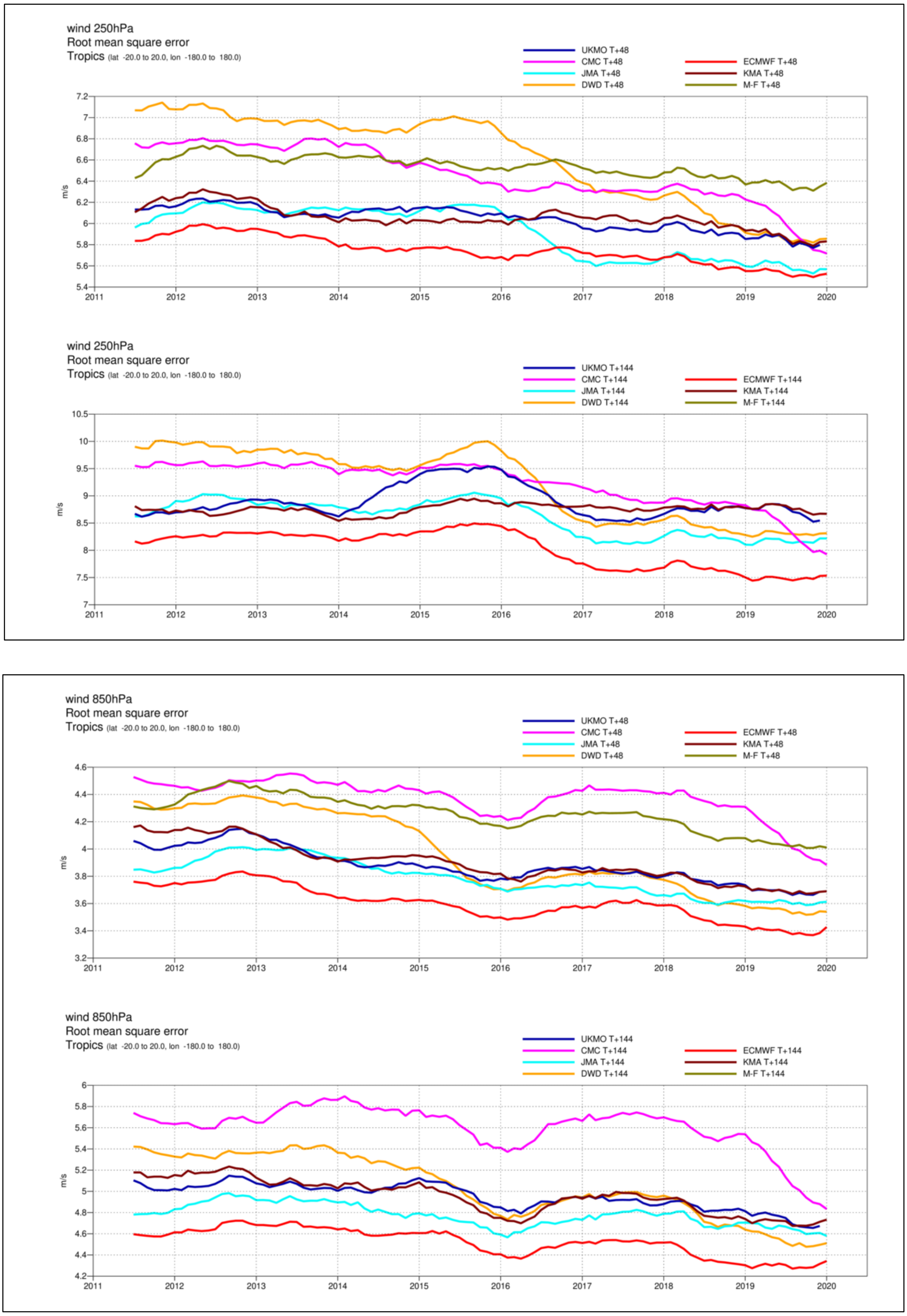

Figure 17**:** As Figure 16 for verification against radiosonde observations.

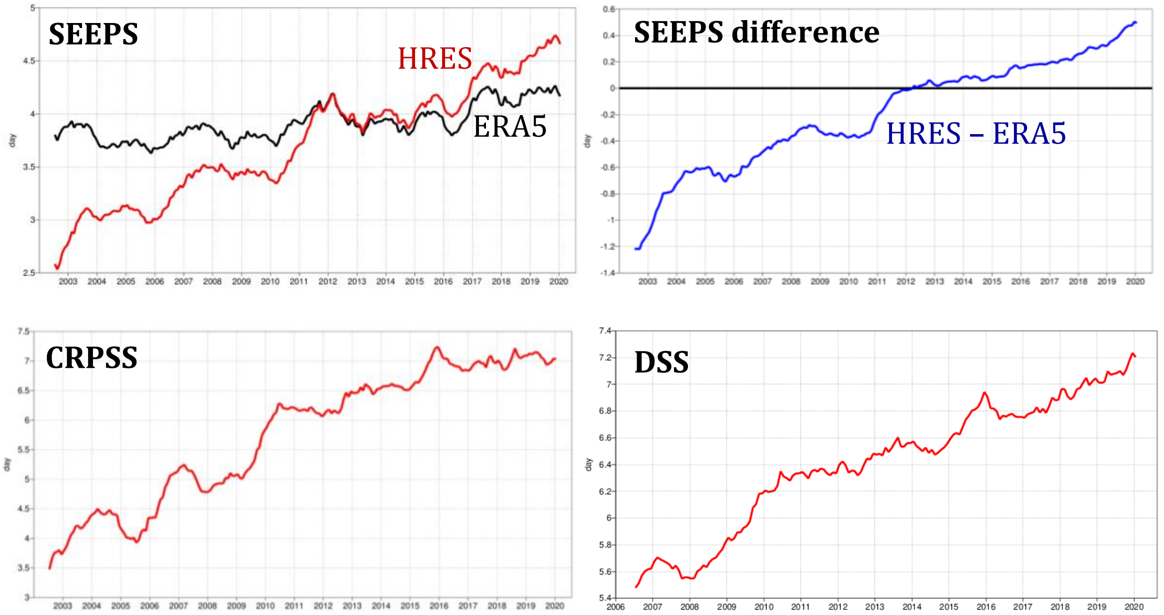

Figure 18**:** Supplementary headline scores (left column) and additional metrics (right column) for deterministic (top) and probabilistic (bottom) precipitation forecasts. The evaluation is for 24-hour total precipitation verified against synoptic observations in the extratropics. Curves show the number of days for which the centred 12-month mean skill remains above a specified threshold. The forecast day on the y-axis is the end of the 24-hour period over which the precipitation is accumulated. The black curve in the top left panel shows the deterministic headline score for ERA5, and the top right panel shows the difference between the operational forecast and ERA5 (blue). Probabilistic scores in the bottom row are the Continuous Ranked Probability Skill Score (CRPSS) and the Diagonal Skill Score (DSS).

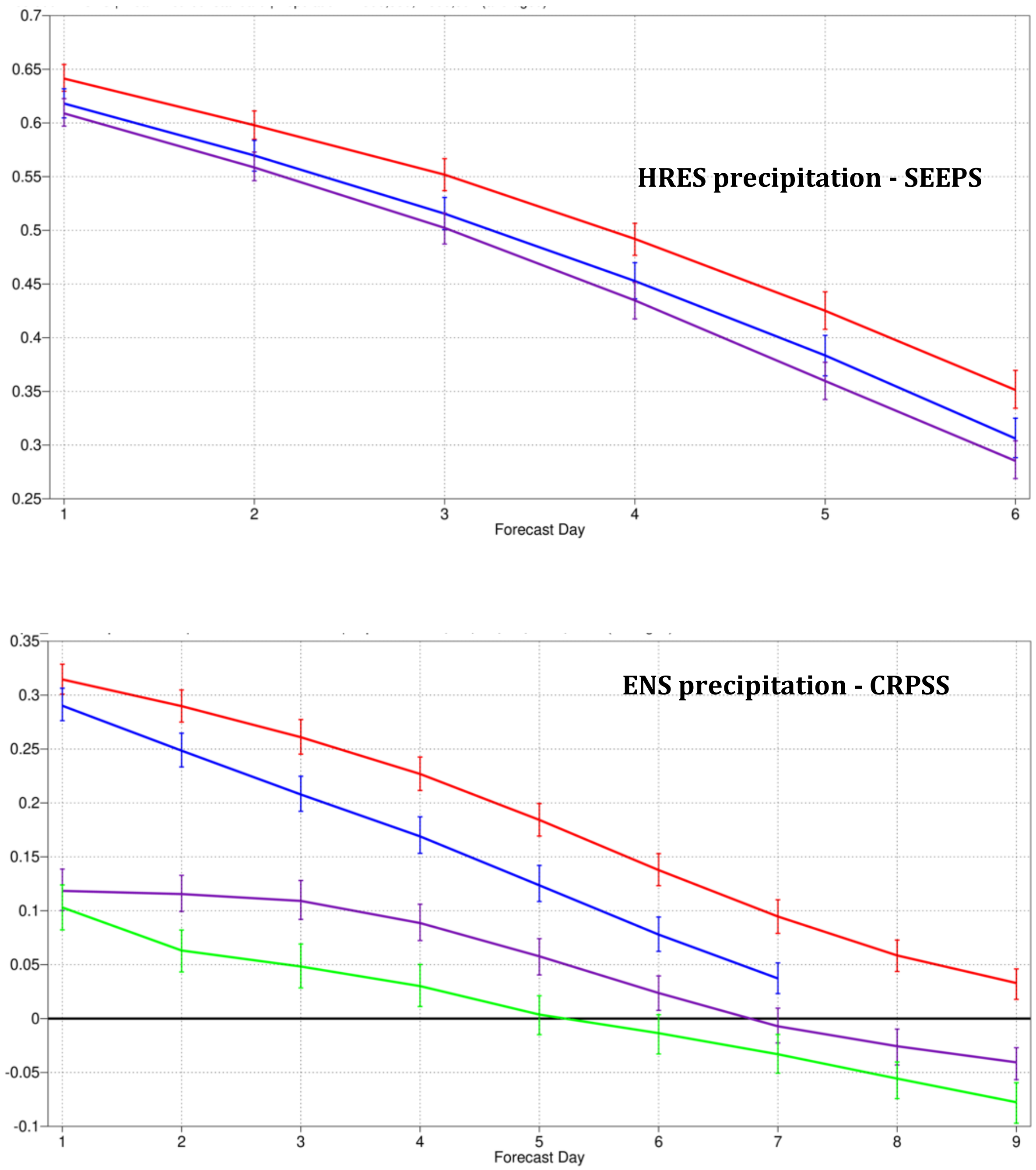

Figure 19**:** Comparison of precipitation forecast skill for ECMWF (red), the Met Office (UKMO, blue), Japan Meteorological Agency (JMA, magenta) and NCEP (green) using the supplementary headline scores for precipitation shown in Figure 18. Top: deterministic; bottom: probabilistic skill. Curves show the skill computed over all available synoptic stations in the extratropics for forecasts from August 2019–July 2020. Bars indicate 95% confidence intervals.

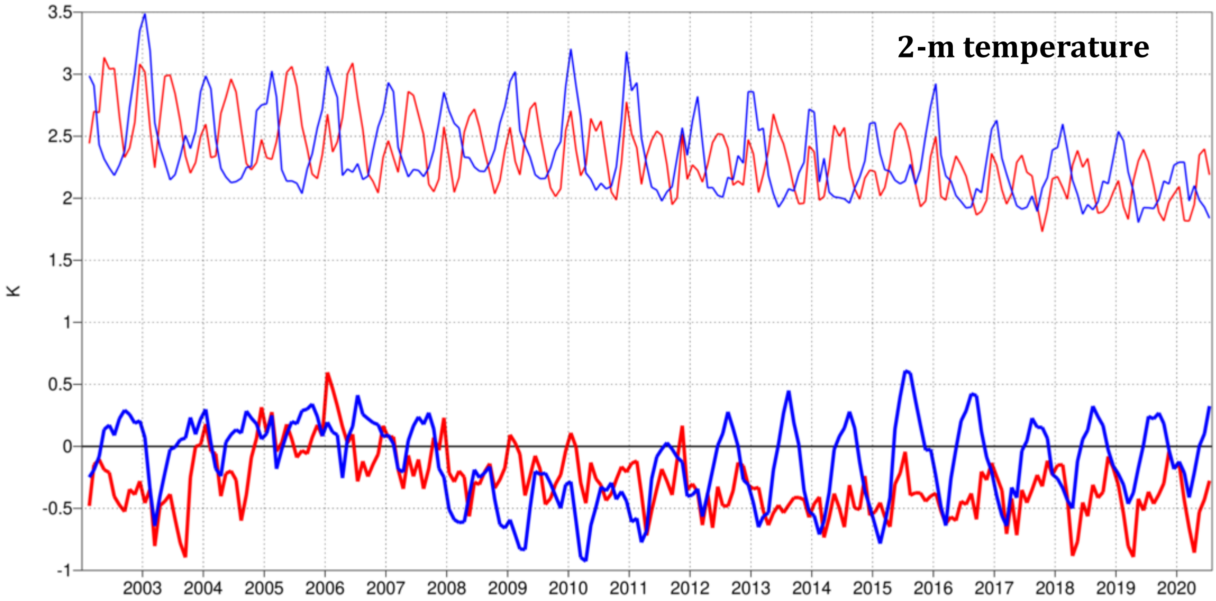

Figure 20**:** Verification of 2 m temperature forecasts against European SYNOP data on the GTS for 60-hour (night-time) and 72-hour (daytime) forecasts. Lower pair of curves shows bias, upper curves are standard deviation of error.

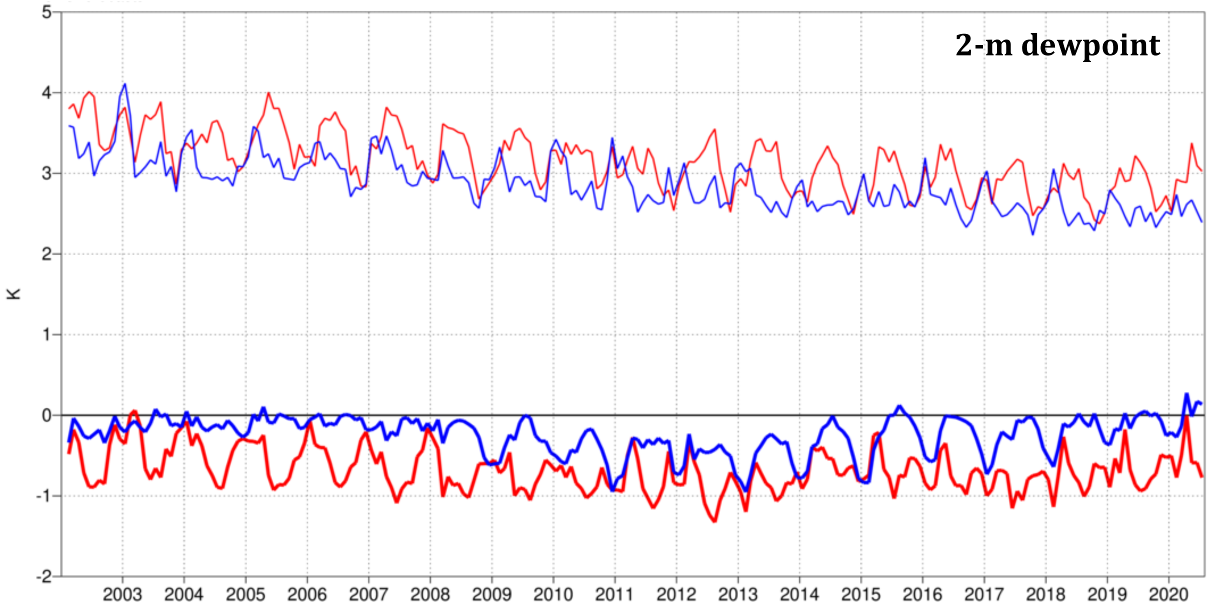

Figure 21**:** Verification of 2 m dew point forecasts against European SYNOP data on the Global Telecommunication System (GTS) for 60-hour (night-time) and 72-hour (daytime) forecasts. Lower pair of curves shows bias, upper curves show standard deviation of error.

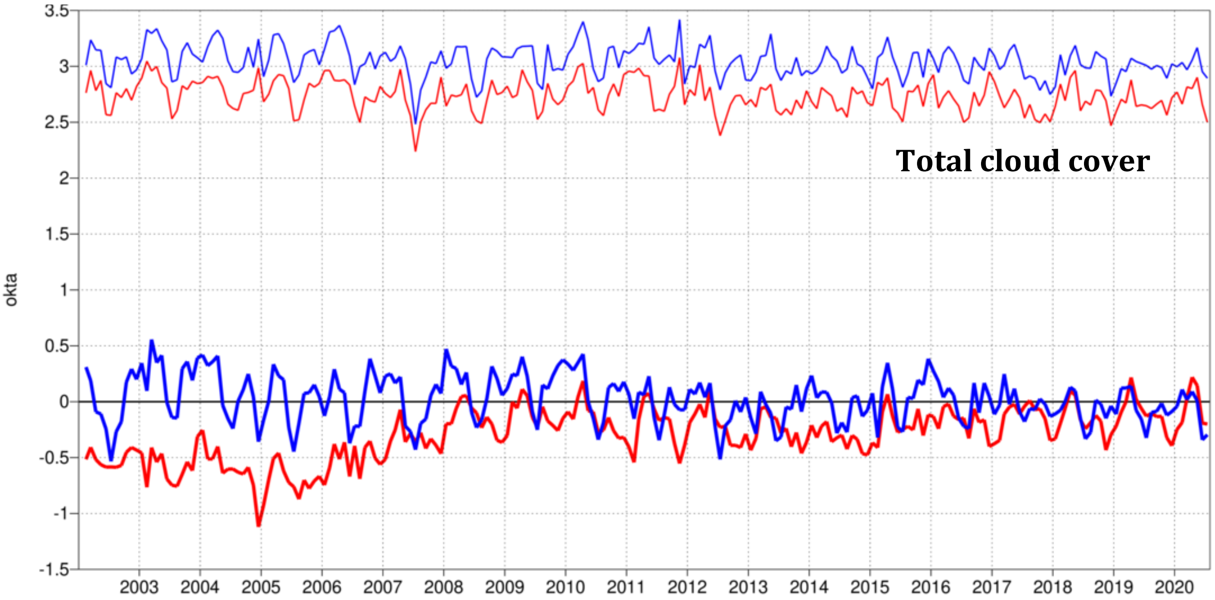

Figure 22**:** Verification of total cloud cover forecasts against European SYNOP data on the GTS for 60-hour (night-time) and 72-hour (daytime) forecasts. Lower pair of curves shows bias, upper curves show standard deviation of error.

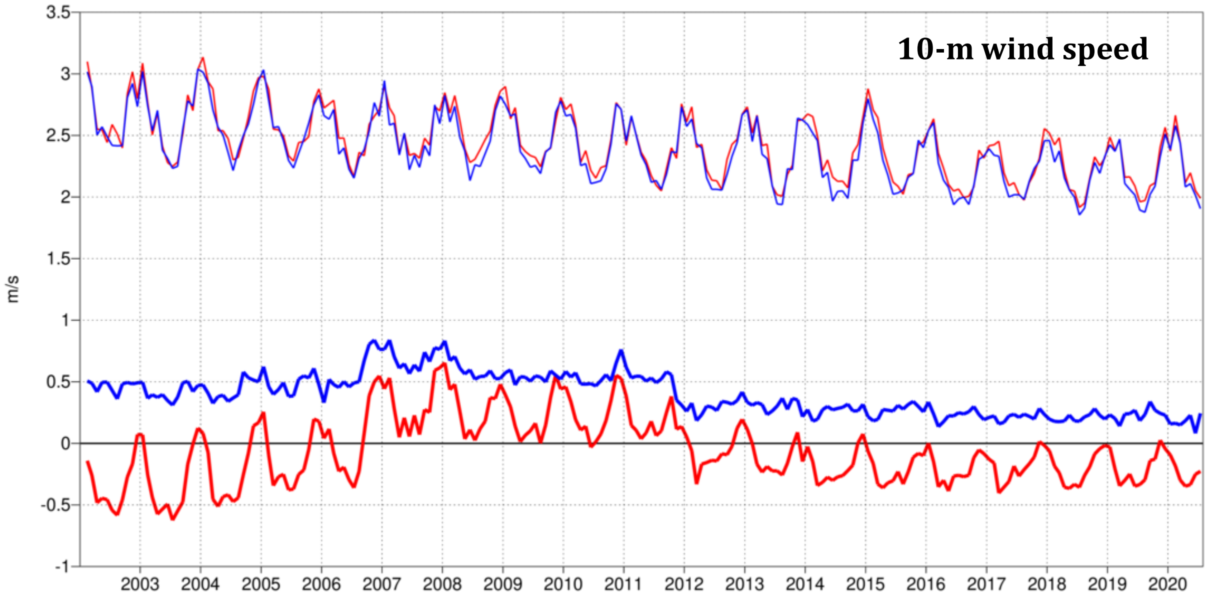

Figure 23**:** Verification of 10 m wind speed forecasts against European SYNOP data on the GTS for 60-hour (night-time) and 72-hour (daytime) forecasts. Lower pair of curves shows bias, upper curves show standard deviation of error.

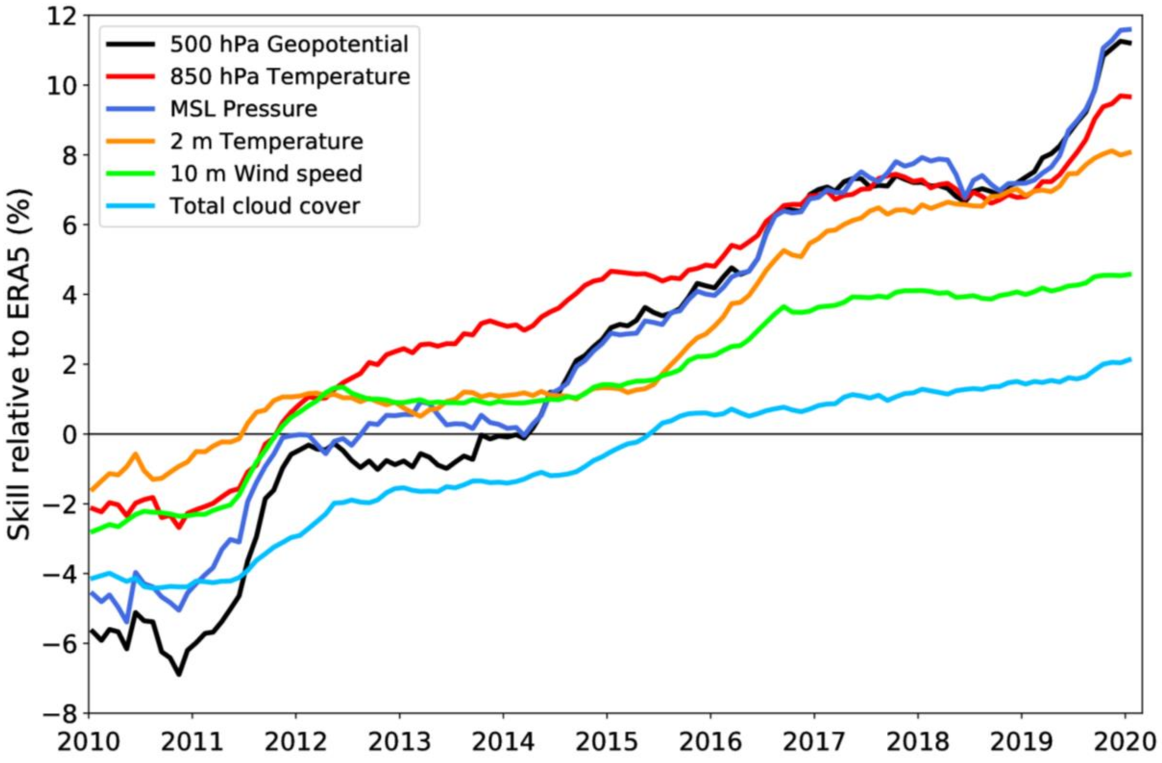

Figure 24: Evolution of skill of the HRES forecast at day 5, expressed as relative skill compared to ERA5. Verification is against analysis for 500 hPa geopotential (Z500), 850 hPa temperature (T850), and mean sea level pressure (MSLP), using error standard deviation as a metric. Verification is against SYNOP for 2 m temperature (T2M), 10 m wind speed (V10), and total cloud cover (TCC).

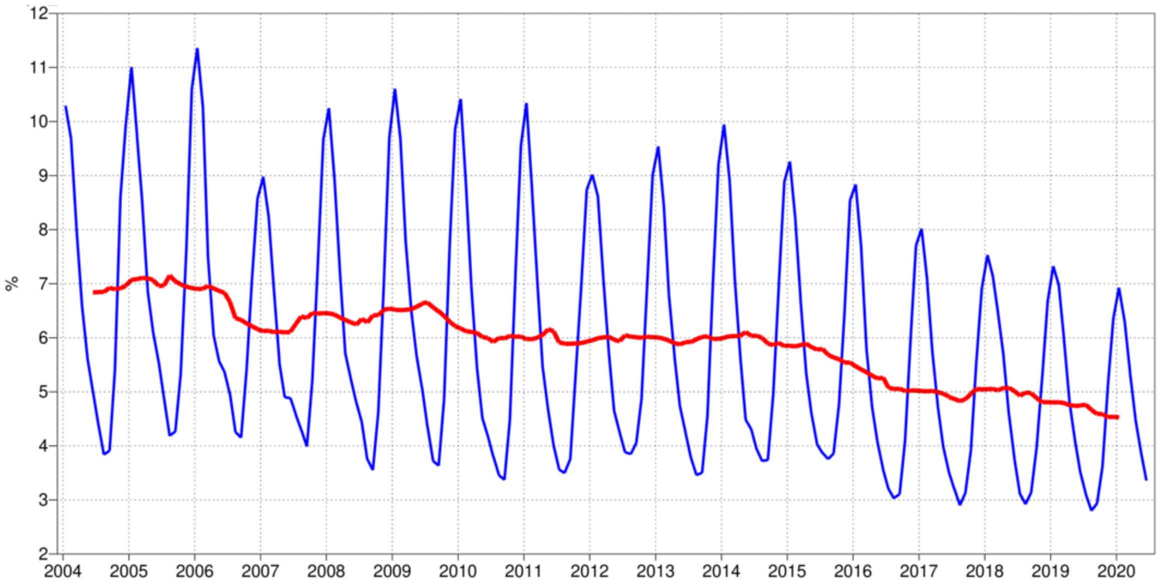

Figure 25: Evolution of the fraction of large 2m temperature errors (CRPS>5K) in the ENS at forecast day 5 in the extratropics. Verification is against SYNOP observations. 12-month running mean shown in red, 3-month running mean in blue.

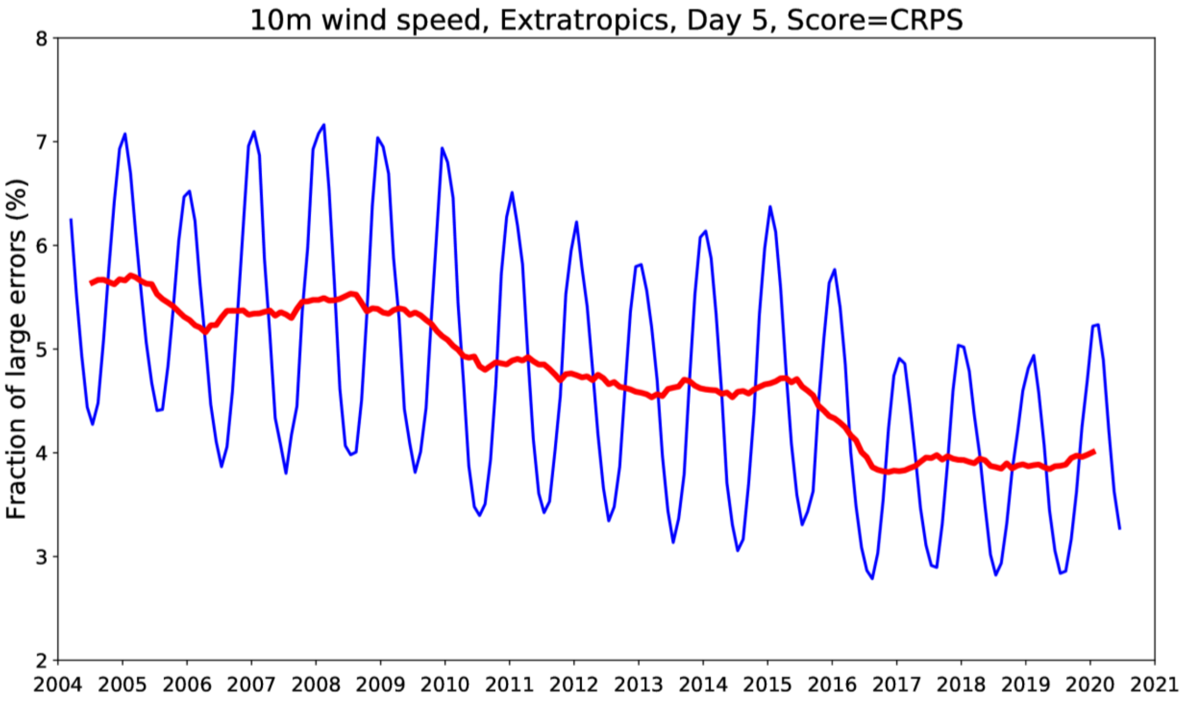

Figure 26: Evolution of the fraction of large 10m wind speed errors (CRPS>4m/s) in the ENS at forecast day 5 in the extratropics. Verification is against SYNOP observations. 12-month running mean shown in red, 3-month running mean in blue.

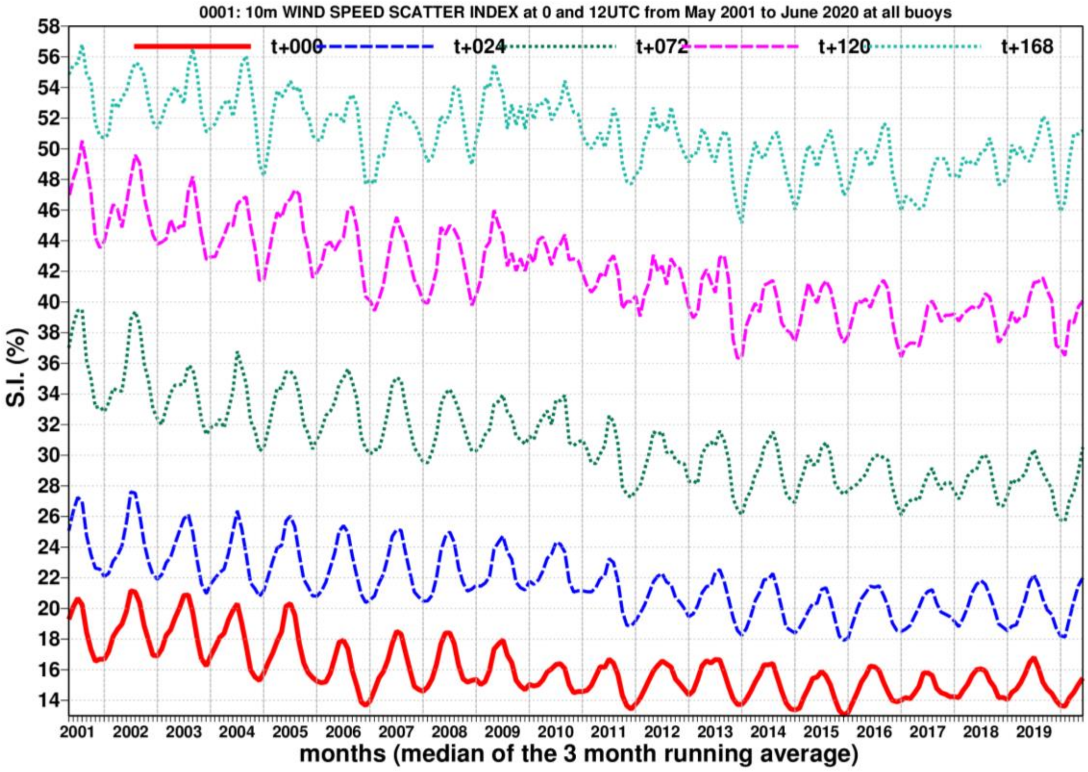

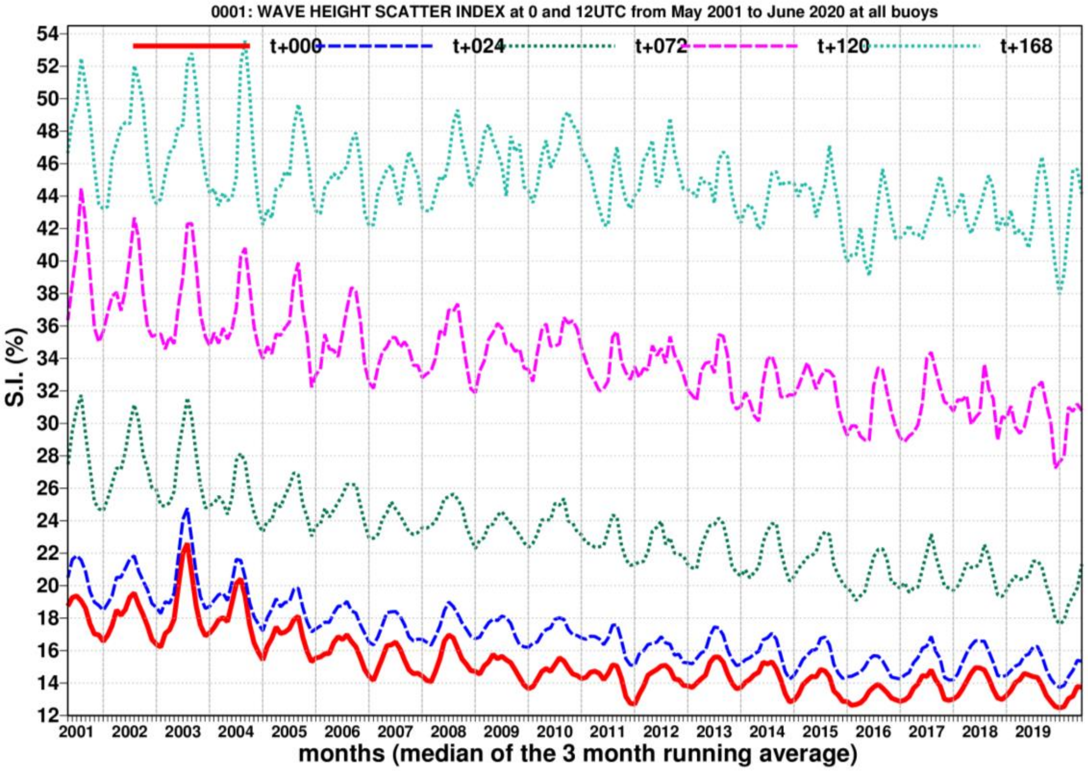

Figure 27: Time series of verification of the ECMWF 10 m wind forecast (top panel) and wave model forecast (wave height, bottom panel) verified against northern hemisphere buoy observations. The scatter index is the error standard deviation normalised by the mean observed value; a three-month running mean is used.

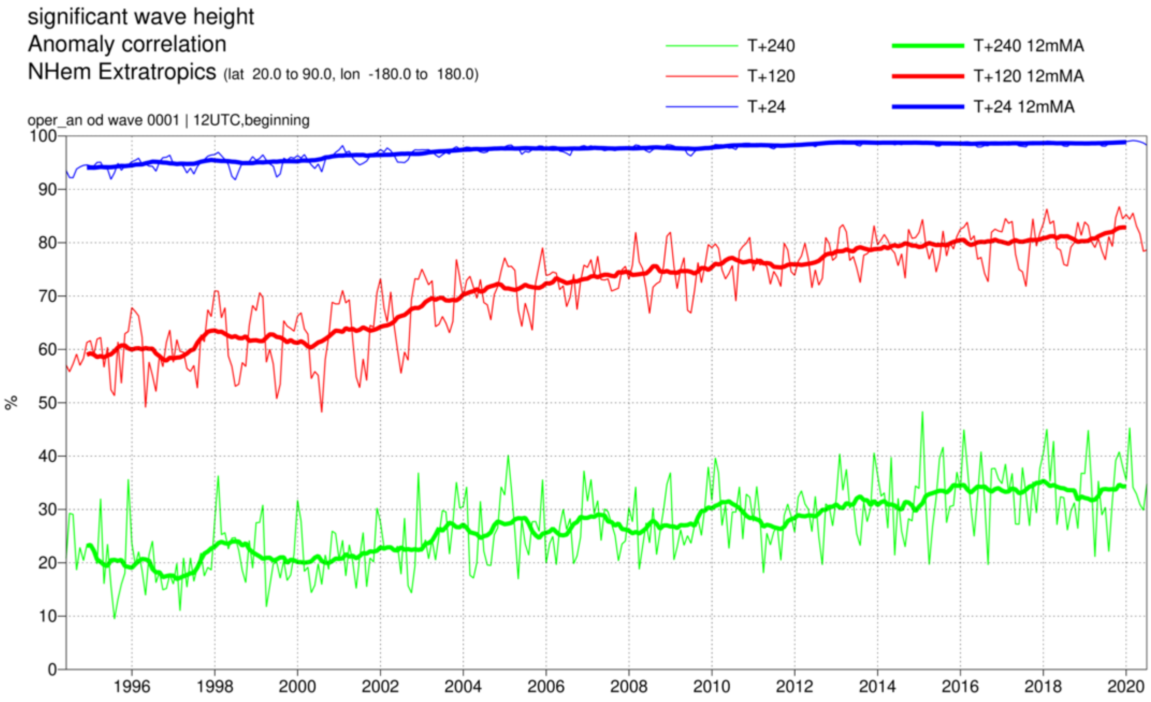

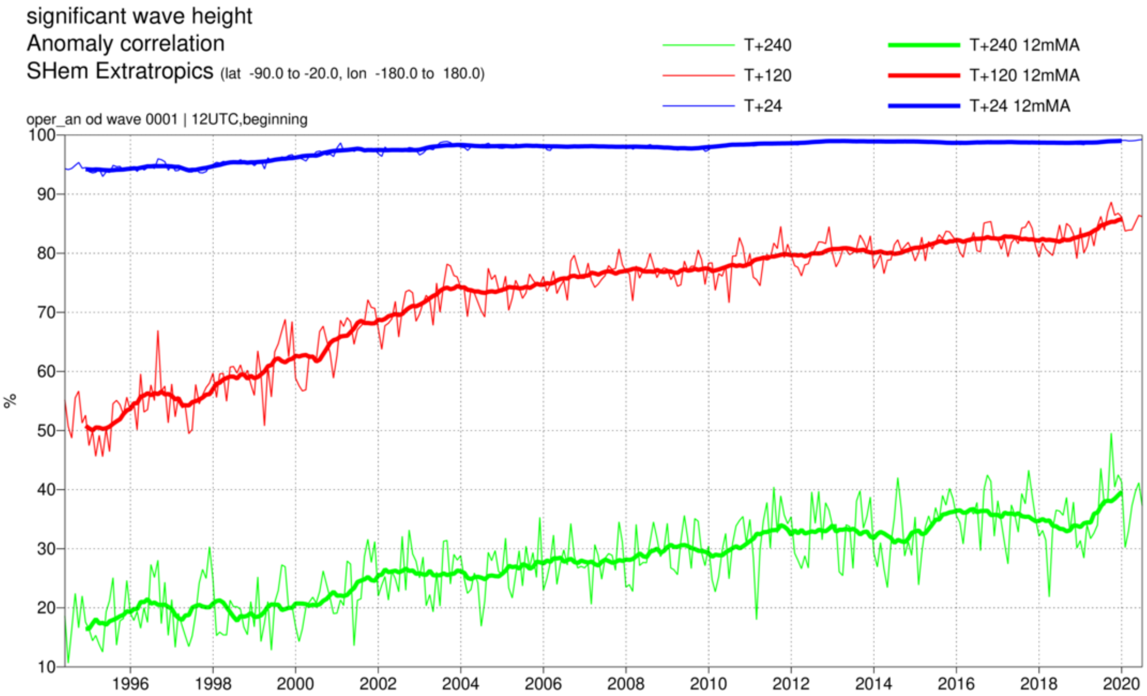

Figure 28: Ocean wave forecasts. Monthly score and 12-month running mean (bold) of ACC for ocean wave heights verified against analysis for the northern (top) and southern extratropics (bottom) at day 1 (blue), 5 (red) and 10 (green).

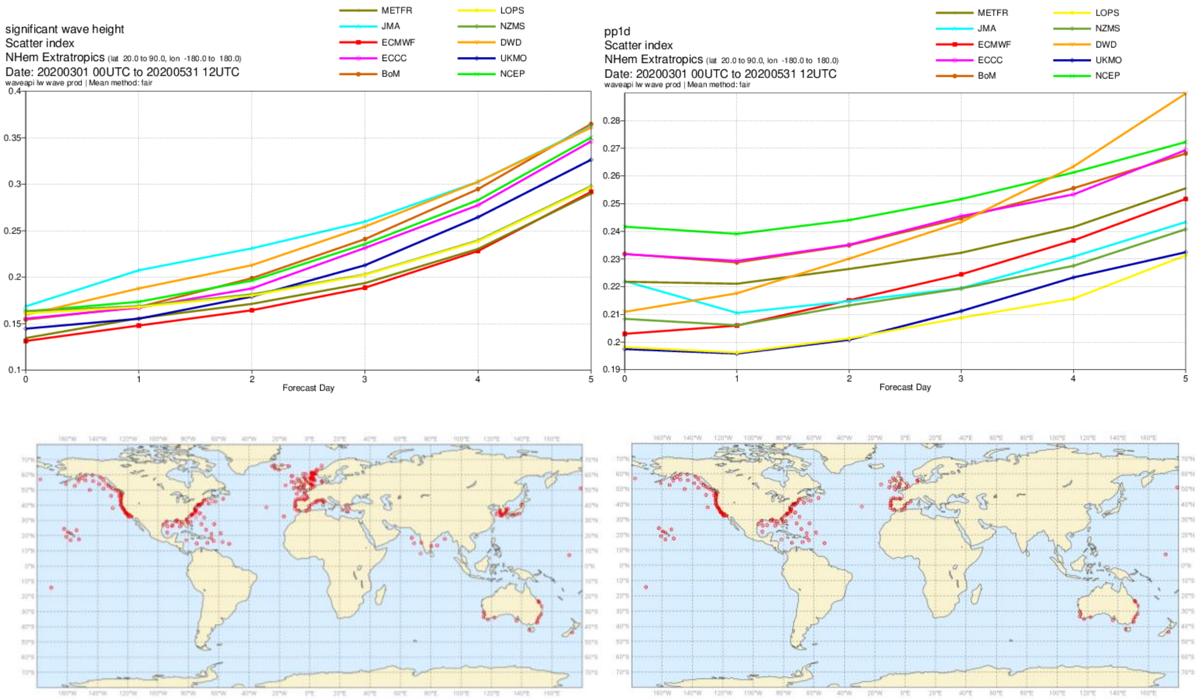

Figure 29: Verification of forecasts of wave height and peak wave period (upper panels) using observations from wave buoys (lower panels). The scatter index (SI) is the standard deviation of error normalised by the mean observed value; plots show the SI for the 3-month period March-May 2020. METFR: Météo-France; JMA: Japan Meteorological Agency; ECCC: Environment and Climate Change Canada; BoM: Bureau of Meteorology, Australia; LOPS: Laboratory for Ocean Physics and Satellite remote sensing, France; NZMS: New Zealand Meteorological Service; DWD: Deutscher Wetterdienst, Germany; UKMO: Met Office, UK; NCEP: National Centers for Environmental Prediction, USA.

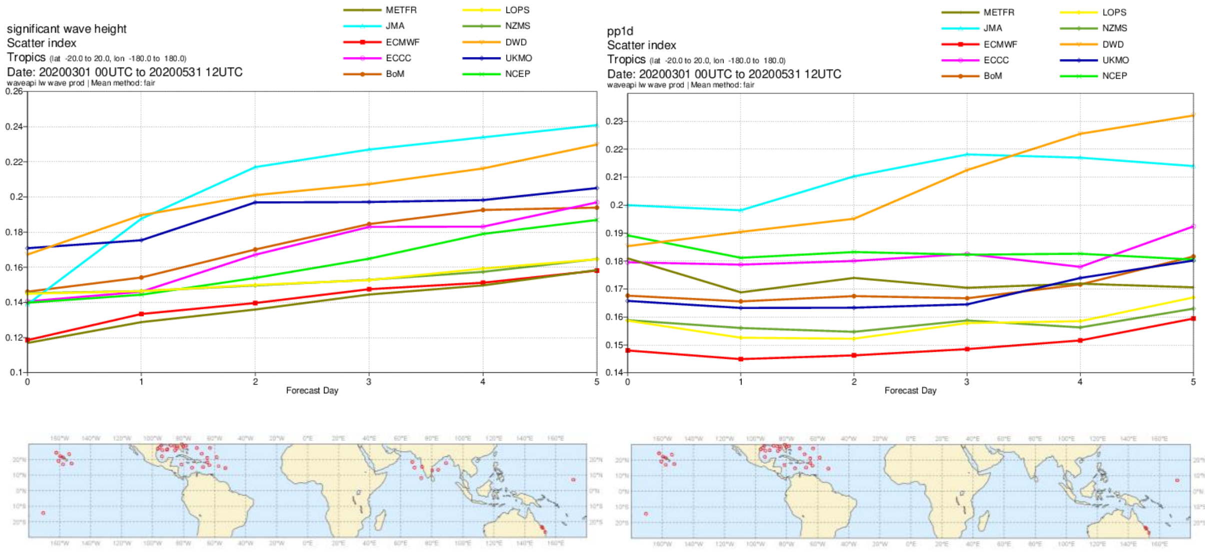

Figure 30: As Figure 29, but for the tropics.

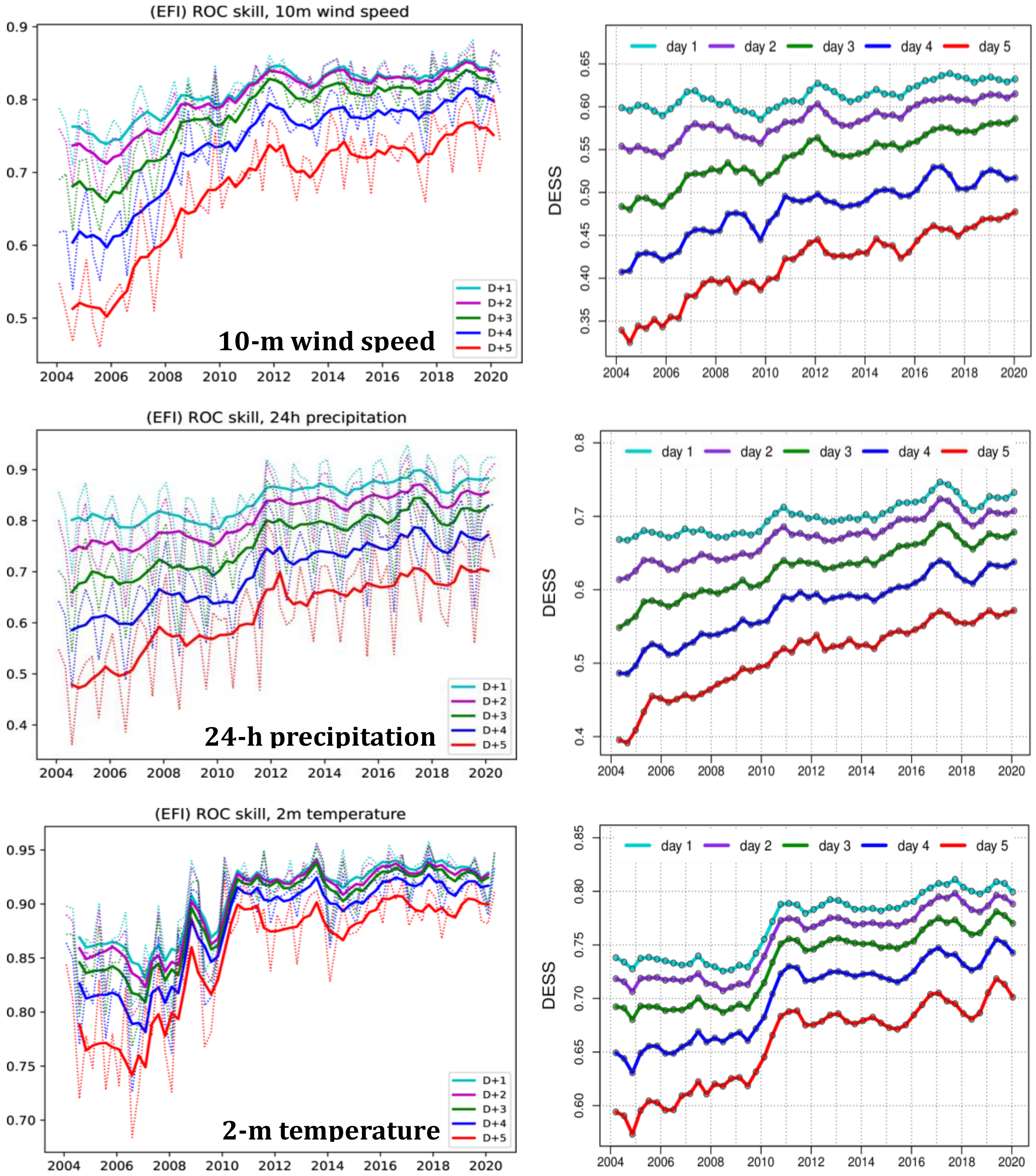

Figure 31: Verification of Extreme Forecast Index (EFI) against analysis (left column). Top panel: skill of the EFI for 10 m wind speed at forecast days 1 (first 24 hours) to 5 (24-hour period 96–120 hours ahead); skill at day 4 (blue line) is the supplementary headline score; an extreme event is taken as an observation exceeding 95th percentile of station climate. Curves show seasonal values (dotted) and four-season running mean (continuous) of relative operating characteristic (ROC) area skill scores. Centre and bottom panels on the left show the equivalent ROC area skill scores for precipitation EFI forecasts and for 2 m temperature EFI forecasts. Diagonal elementary skill score (DESS) for the 95th percentile for the same three variables, taking observation uncertainty into account (right column).

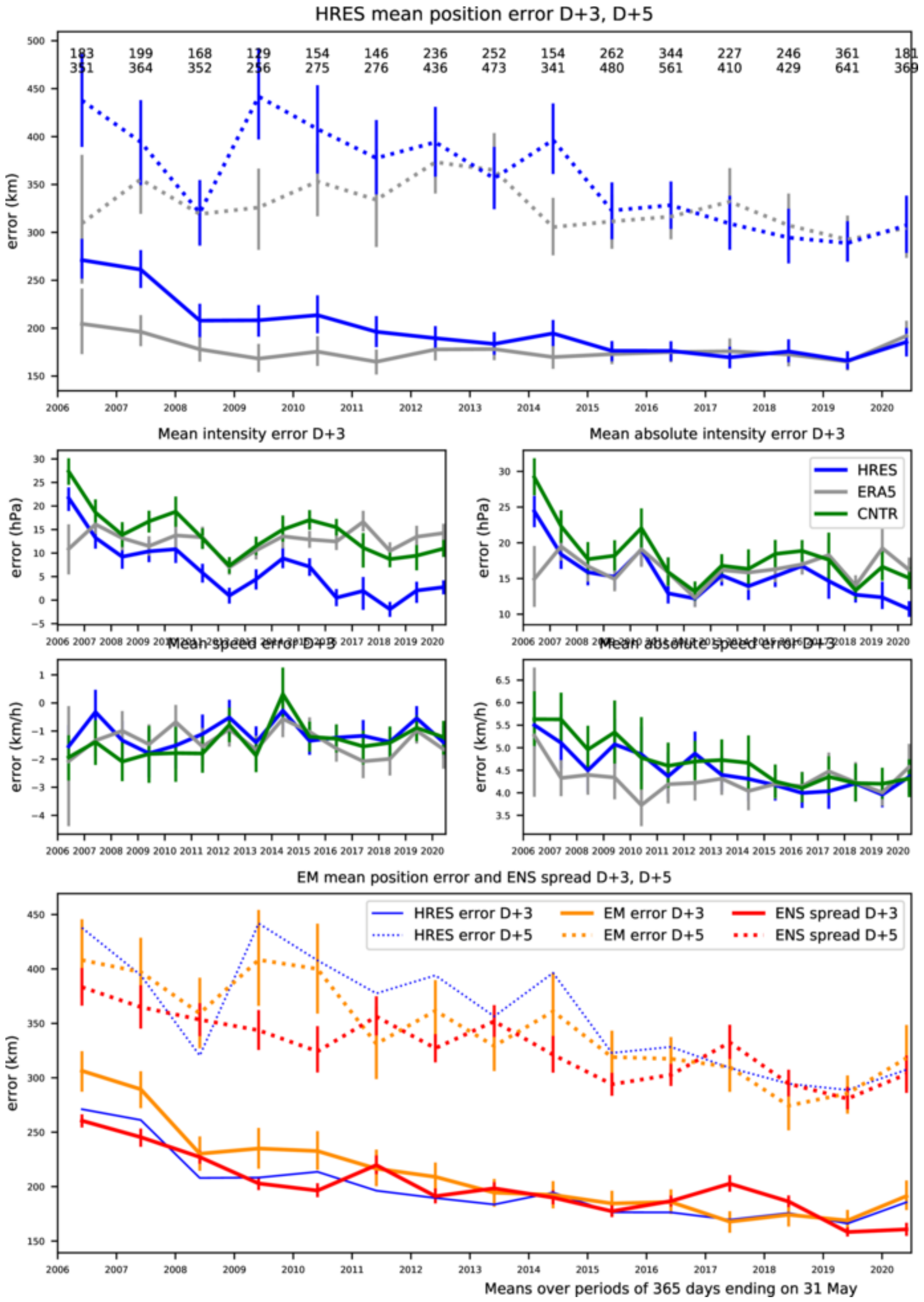

Figure 32: Verification of tropical cyclone predictions from the operational high-resolution and ensemble forecast. Results are shown for all tropical cyclones occurring globally in 12-month periods ending on 31 May. Verification is against the observed position reported via the GTS. Top panel supplementary headline score – the mean position error (km) of the three-day high-resolution forecast. The error for day 5 is included for comparison. Centre four panels show mean error (bias) in the cyclone intensity (difference between forecast and reported central pressure; positive error indicates the forecast pressure is less deep than observed), mean absolute error of the intensity and mean and absolute error of cyclone motion speed for cyclone forecast both by HRES and ENS control. Bottom panel shows mean position error of ensemble mean (mean of cyclones forecast by ensemble members) with respect to the observed cyclone (orange curve) and ensemble spread (mean of distances of ensemble cyclones from the ensemble mean; red curve); for comparison the HRES position error (from the top panel) is plotted as well (blue curve). For reference, errors of tropical cyclone forecasts by ERA5 are shown in grey.

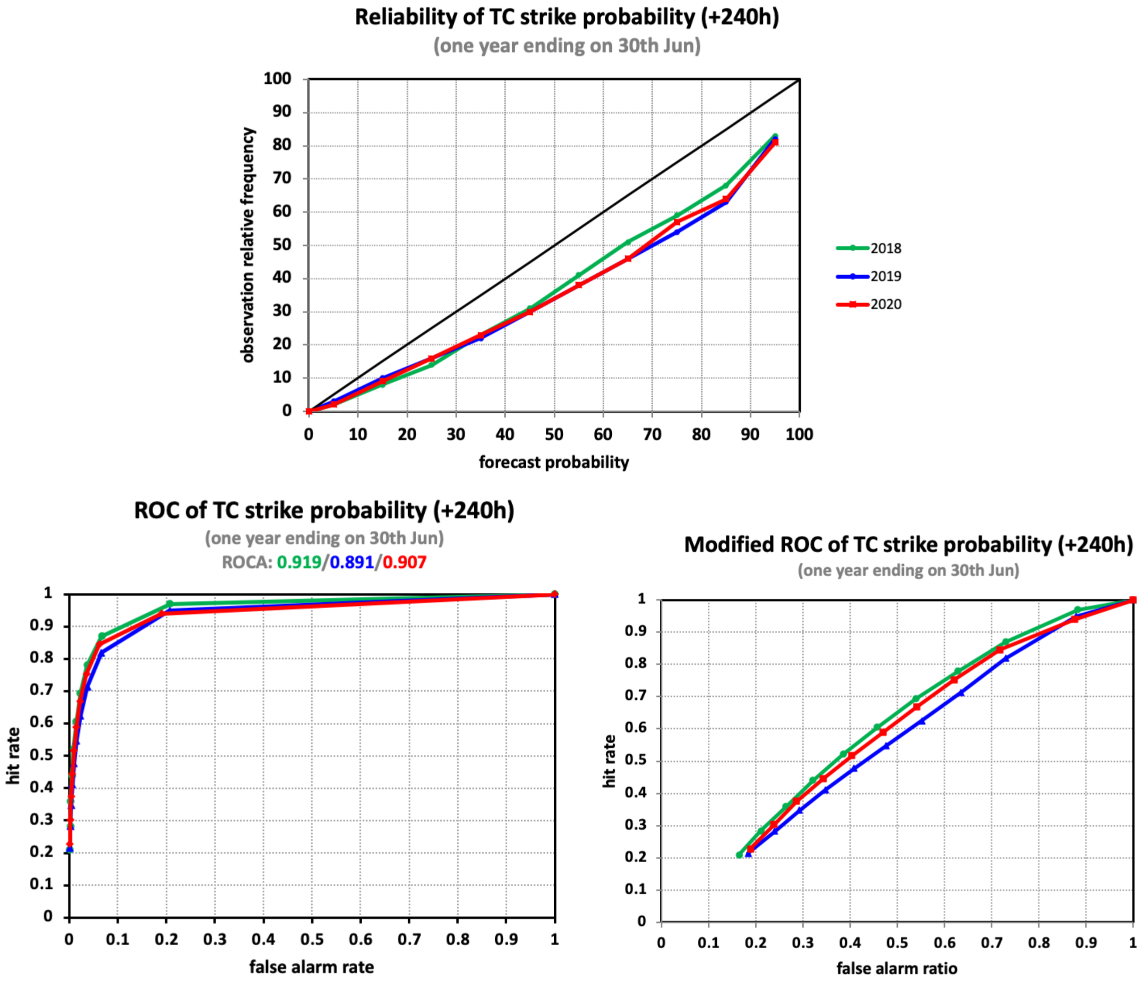

Figure 33: Probabilistic verification of ensemble tropical cyclone forecasts at day 10 for three 12-month periods: July 2017–June 2018 (green), July 2018–June 2019 (blue) and July 2019–June 2020 (red). Upper panel shows reliability diagram (the closer to the diagonal, the better). The lower panel shows (left) the standard ROC diagram and (right) a modified ROC diagram, where the false alarm ratio is used instead of the false alarm rate. For both ROC and modified ROC, the closer the curve is to the upper-left corner, the better, indicating a greater proportion of hits, and fewer false alarms.

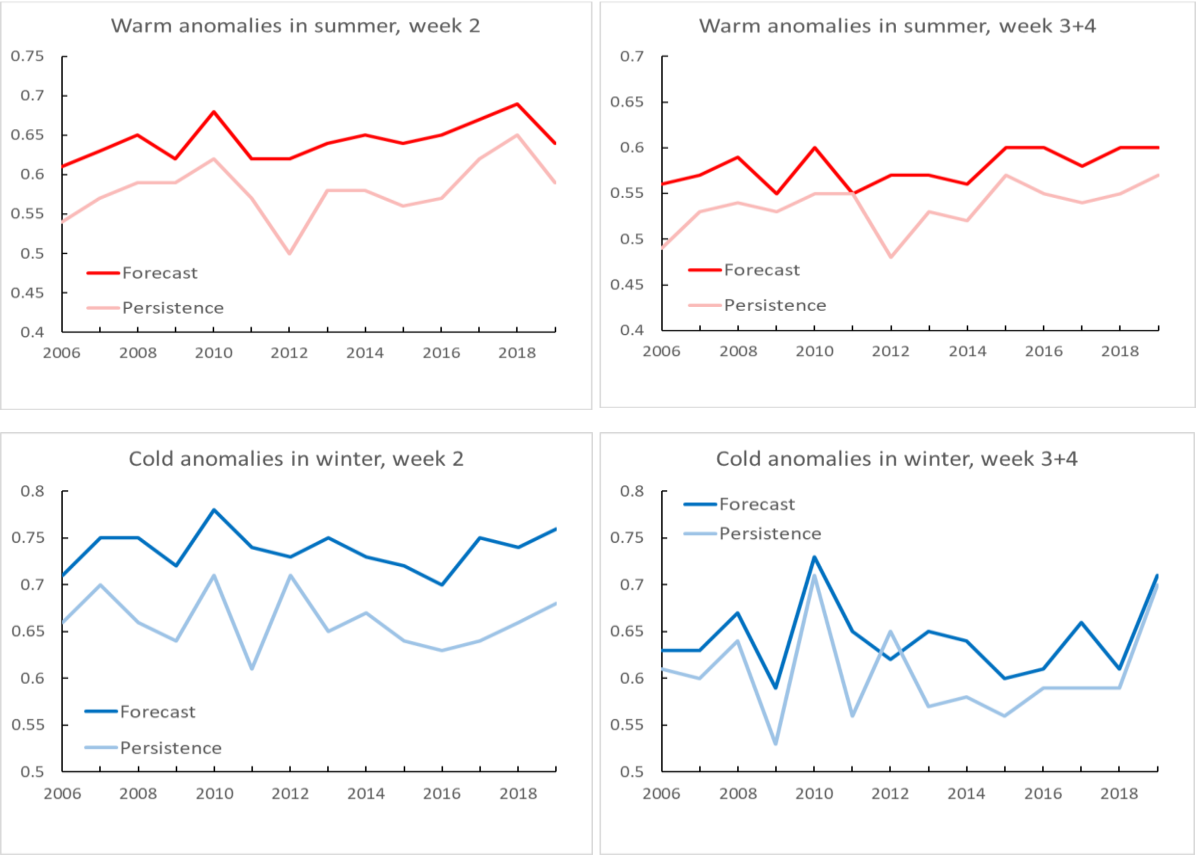

Figure 34**:** Verification of the monthly forecast against analysis. Area under the ROC curve for the probability that 2 m temperature is in the upper third of the climate distribution in summer (top) and in the lower third in winter (bottom). Scores are calculated for each three-month season for all land points in the extra-tropical northern hemisphere. Left panels show the score of the operational monthly forecasting system for forecast days 12–18 (7-day mean), and right panels for forecast days 19–32 (14-day mean). As a reference, lighter coloured lines show the score using persistence of the preceding 7-day or 14-day period of the forecast.

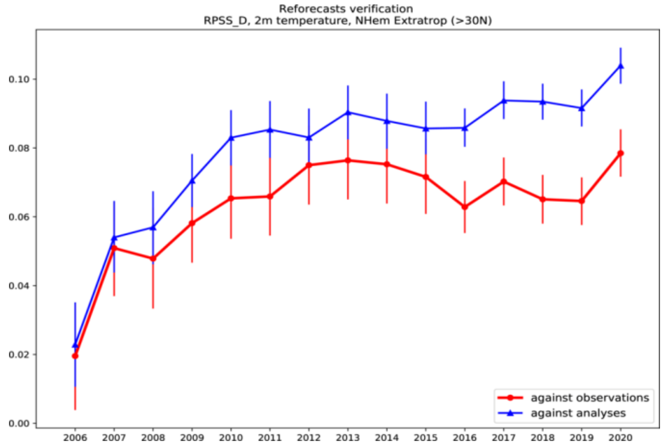

Figure 35: Skill of the ENS in predicting weekly mean 2m temperature anomalies (terciles) in week 3 in the northern extratropics. Verification against own analysis shown in blue, verification against SYNOP observations shown in red. Verification metric is the Ranked Probability Skill Score.

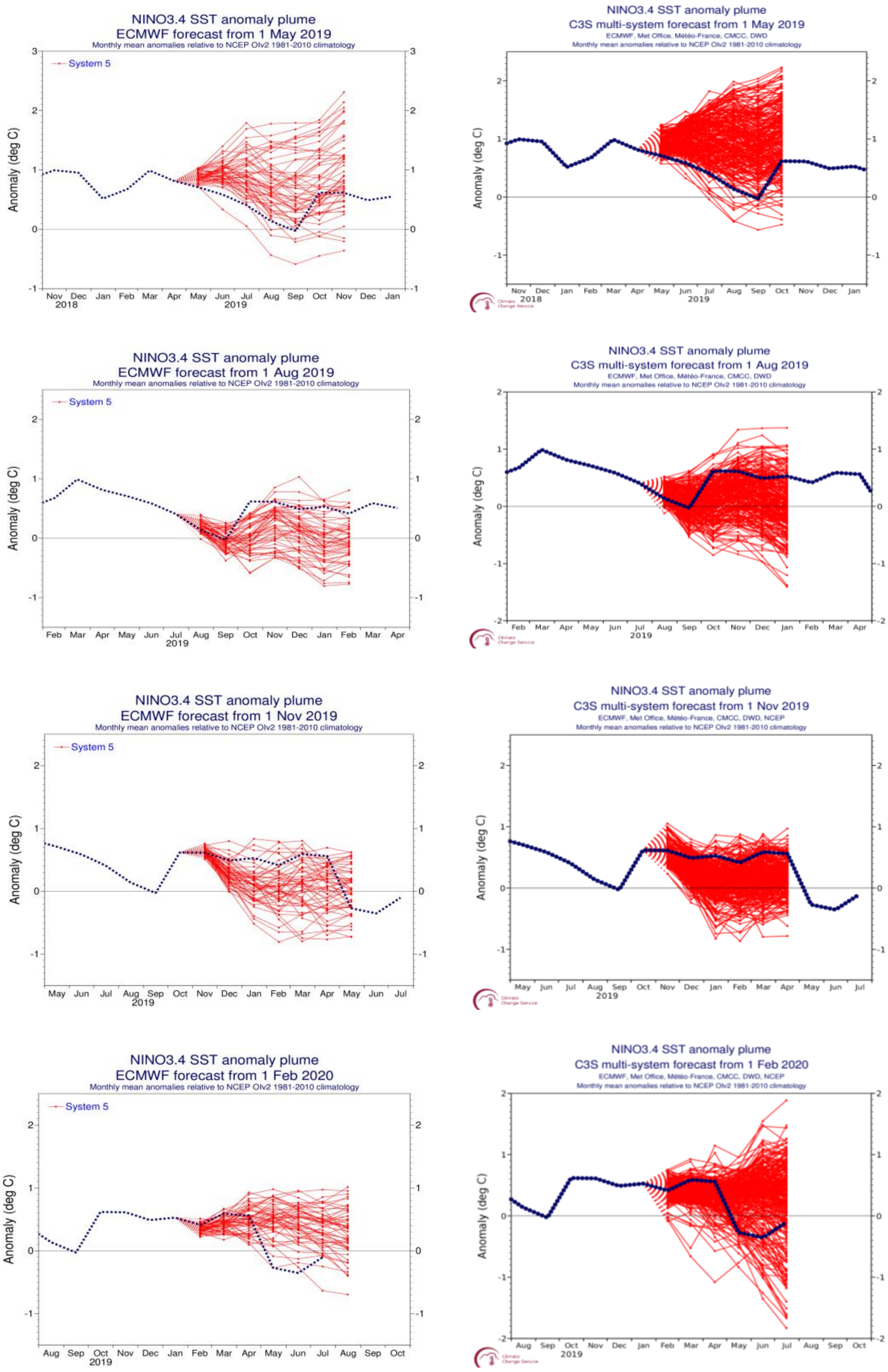

NINO3.4 SST anomaly plume
ECMWF forecast from 1 May 2019
Monthly mean anomalies relative to NCEP OIv2 1981-2010 climatology

NINO3.4 SST anomaly plume
C3S multi-system forecast from 1 May 2019
ECMWF, Met Office, Météo-France, CMCC, DWD
Monthly mean anomalies relative to NCEP OIv2 1981-2010 climatology

NINO3.4 SST anomaly plume
ECMWF forecast from 1 Aug 2019
Monthly mean anomalies relative to NCEP OIv2 1981-2010 climatology

NINO3.4 SST anomaly plume
C3S multi-system forecast from 1 Aug 2019
ECMWF, Met Office, Météo-France, CMCC, DWD
Monthly mean anomalies relative to NCEP OIv2 1981-2010 climatology

NINO3.4 SST anomaly plume
ECMWF forecast from 1 Nov 2019
Monthly mean anomalies relative to NCEP OIv2 1981-2010 climatology

NINO3.4 SST anomaly plume
C3S multi-system forecast from 1 Nov 2019
ECMWF, Met Office, Météo-France, CMCC, DWD, NCEP
Monthly mean anomalies relative to NCEP OIv2 1981-2010 climatology

NINO3.4 SST anomaly plume
ECMWF forecast from 1 Feb 2020
Monthly mean anomalies relative to NCEP OIv2 1981-2010 climatology

NINO3.4 SST anomaly plume
C3S multi-system forecast from 1 Feb 2020
ECMWF, Met Office, Météo-France, CMCC, DWD, NCEP
Monthly mean anomalies relative to NCEP OIv2 1981-2010 climatology

System 5
Anomaly (deg C)
Nov Dec Jan Feb Mar Apr May Jun Jul Aug Sep Oct Nov Dec Jan
2018
2019
Feb Mar Apr May Jun Jul Aug Sep Oct Nov Dec Jan Feb Mar Apr
May Jun Jul Aug Sep Oct Nov Dec Jan Feb Mar Apr May Jun Jul
Aug Sep Oct Nov Dec Jan Feb Mar Apr May Jun Jul Aug Sep Oct
Climate Change Service

Figure 36: ECMWF System 5 (left column), and Copernicus Climate Change Service multi-model (right column) seasonal forecasts of SST anomalies over the NINO 3.4 region of the tropical Pacific from (top to bottom rows) May 2019, August 2019, November 2019 and February 2020. The red lines represent the ensemble members; dotted blue line shows the subsequent verification. The C3S multi-model forecast includes forecasts from ECMWF, MetOffice, Meteo-France, CMCC, DWD, and NCEP.

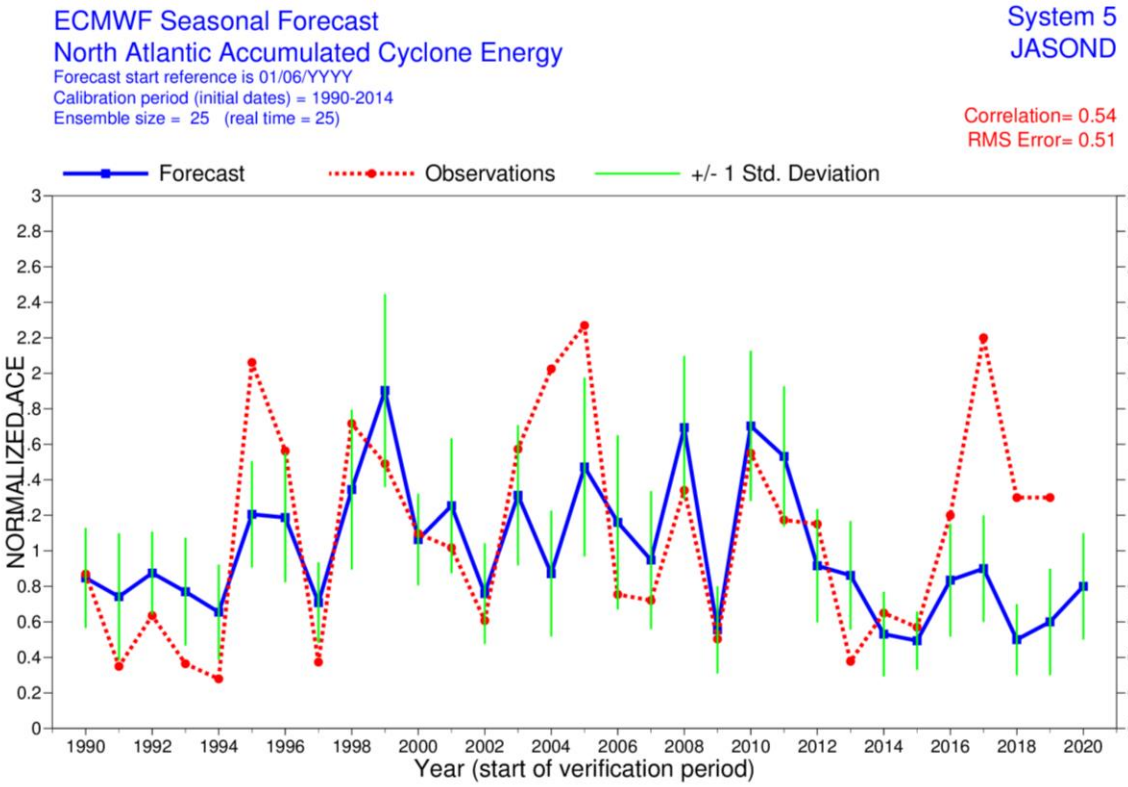

Figure 37: Time series of accumulated cyclone energy (ACE) for the Atlantic tropical storm seasons July–December 1990 to July–December 2019. Blue line indicates the ensemble mean forecasts and green bars show the associated uncertainty (±1 standard deviation); red dotted line shows observations. Forecasts are from SEAS5 of the seasonal component of the IFS: these are based on the 25-member re-forecasts; from 2017 onwards, they are from the operational 51-member seasonal forecast ensemble. Start date of the forecast is 1 June.

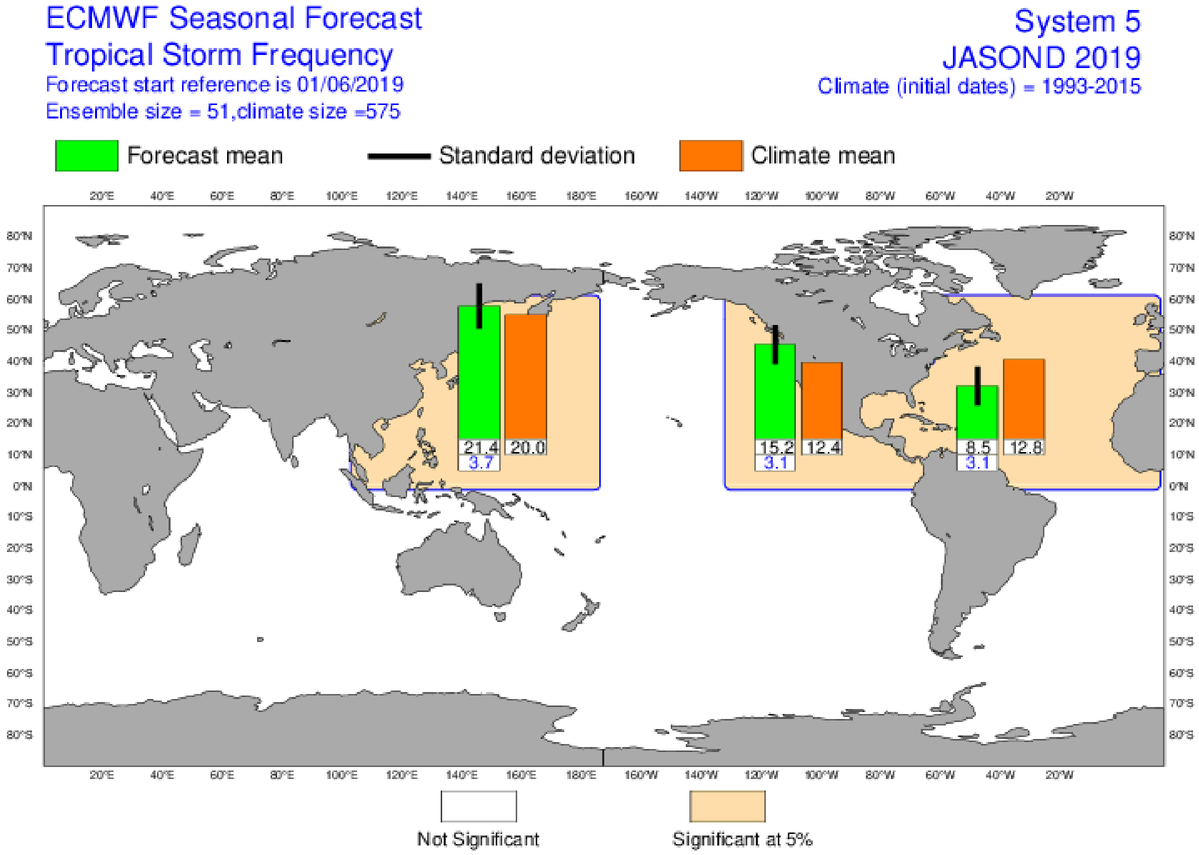

Figure 38: Tropical storm frequency forecast issued in June 2019 for the six-month period July–December 2019. Green bars represent the forecast number of tropical storms in each ocean basin (ensemble mean); orange bars represent climatology. The values of each bar are written in black underneath. The black bars represent ±1 standard deviation within the ensemble distribution; these values are indicated by the blue number. The 51-member ensemble forecast is compared with the climatology. A Wilcoxon-Mann-Whitney (WMW) test is then applied to evaluate if the predicted tropical storm frequencies are significantly different from the climatology. The ocean basins where the WMW test detects significance larger than 90% have a shaded background.

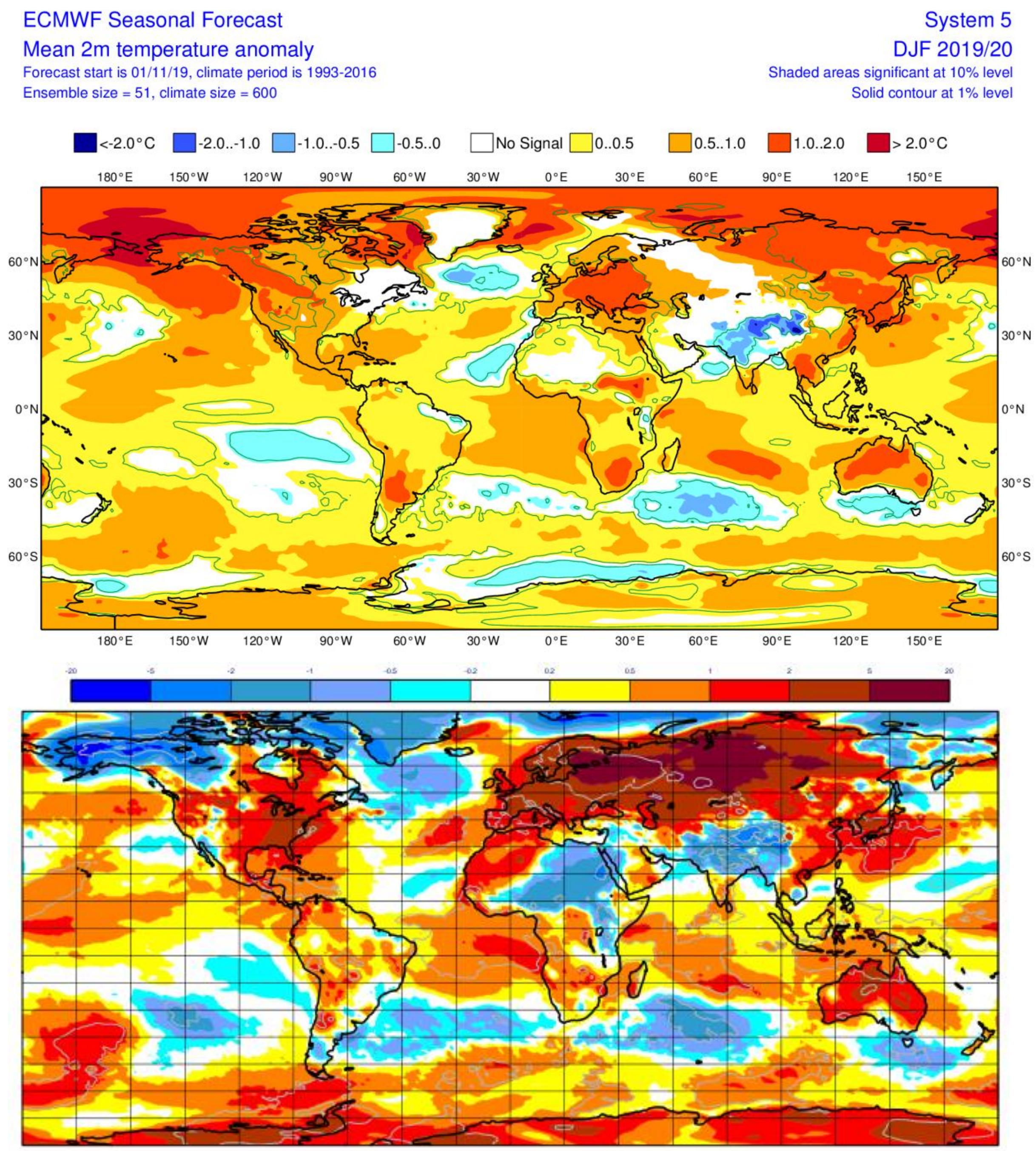

Figure 39**:** Anomaly of 2 m temperature as predicted by the seasonal forecast from November 2019 for DJF 2019/20 (upper panel) and verifying analysis (lower panel). Grey contours in the analysis indicate regions where anomalies exceed 1.5 standard deviations.

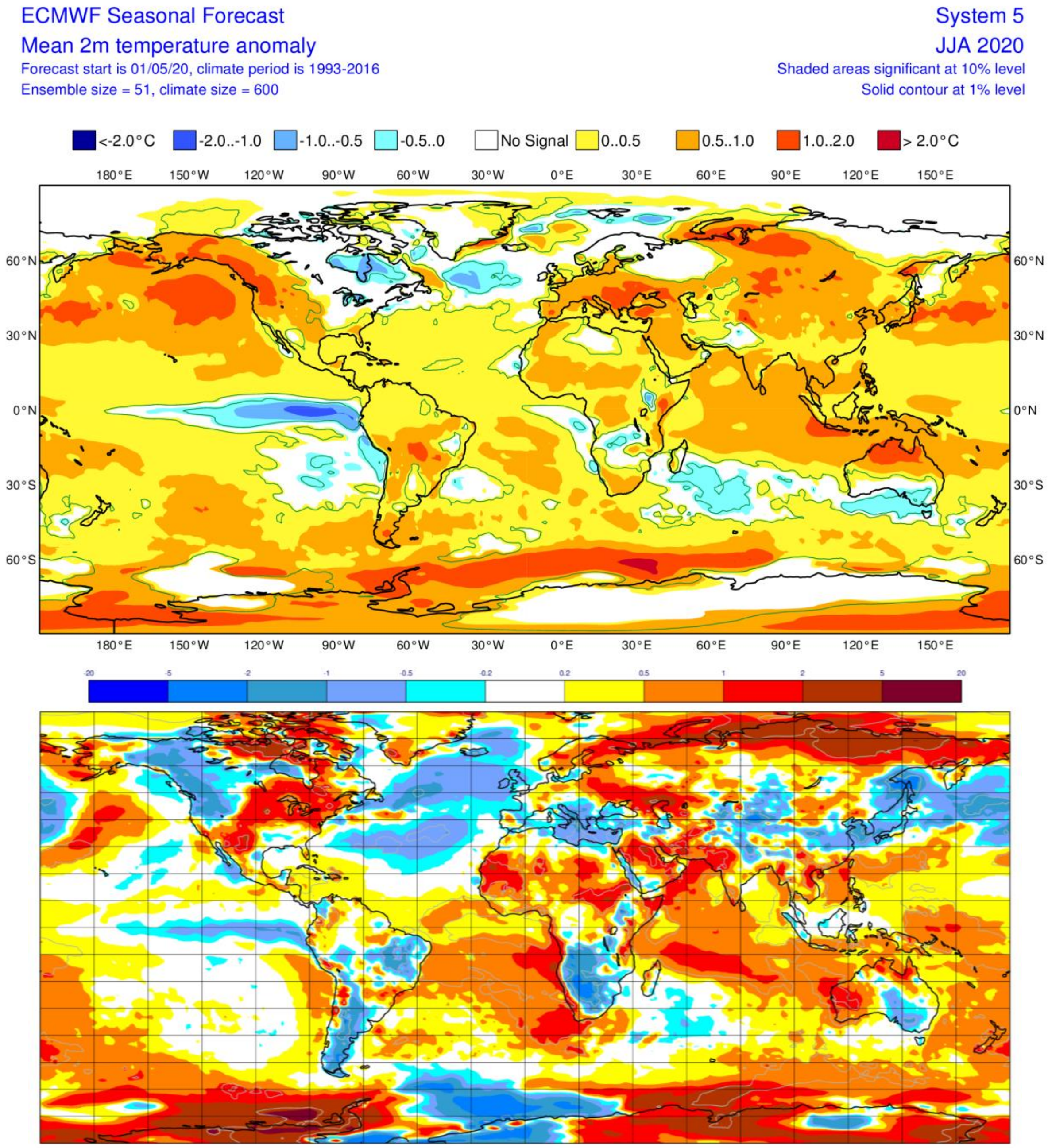

Figure 40: Anomaly of 2 m temperature as predicted by the seasonal forecast from May 2020 for JJA 2020 (upper panel) and verifying analysis (lower panel). Grey contours in the analysis indicate regions where anomalies exceed 1.5 standard deviations.

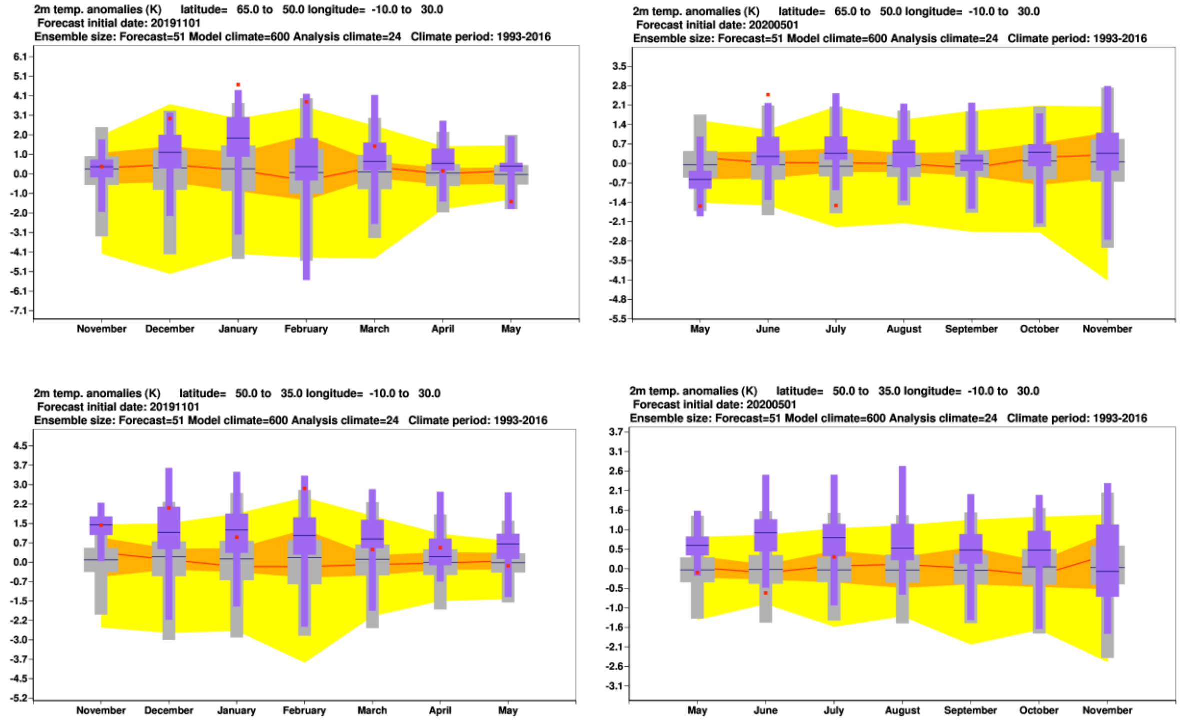

Figure 41: Long-range forecast of 2 m temperature anomalies from November 2019 for DJF 2019–20 (left panels) and from May 2020 for JJA 2020 (right panels) for northern (top) and southern Europe (bottom). The forecast is shown in purple, the model climatology derived from the System-5 hindcasts is shown in grey, and the analysis in the 24-year hindcast period is shown in yellow and orange. The limits of the purple/grey whiskers and yellow band correspond to the 5th and 95th percentiles, those of the purple/grey box and orange band to the lower and upper tercile, and medians are represented by lines. The verification from operational analyses is shown as a red square. Areal averages have been computed using land fraction as a weight, in order to isolate temperature variations over land.

A short note on scores used in this report

A. 1 Deterministic upper-air forecasts

The verifications used follow WMO CBS recommendations as closely as possible. Scores are computed from forecasts on a standard 1.5 × 1.5 grid (computed from spectral fields with T120 truncation) limited to standard domains (bounding co-ordinates are reproduced in the figure inner captions), as this is the resolution agreed in the updated WMO CBS recommendations approved by the 16th WMO Congress in 2011. When other centres' scores are produced, they have been provided as part of the WMO CBS exchange of scores among GDPS centres, unless stated otherwise – e.g. when verification scores are computed using radiosonde data (Figure 14), the sondes have been selected following an agreement reached by data monitoring centres and published in the WMO WWW Operational Newsletter.

Root mean square errors (RMSE) are the square root of the geographical average of the squared differences between the forecast field and the analysis valid for the same time. When models are compared, each model uses its own analysis for verification; RMSE for winds (Figure 14, Figure 16) are computed by taking the root of the sums of the mean squared errors for the two components of the wind independently.

Skill scores are computed as the reduction in RMSE achieved by the model with respect to persistence (forecast obtained by persisting the initial analysis over the forecast range); in mathematical terms:

$$\mathrm{SS} = 100 * \left(1 - \frac{\mathrm{RMSE}_f^2}{\mathrm{RMSE}_p^2}\right)$$

Figure 3 shows correlations in space between the forecast anomaly and the verifying analysis anomaly. Anomalies with respect to ERA-Interim analysis climate are available at ECMWF from early 1980s. For ocean waves (Figure 28) the climate has been also derived from the ERA-Interim analyses.

A. 2 Probabilistic forecasts

Events for the verification of medium-range probabilistic forecasts are usually defined as anomalies with reference to a suitable climatology. For upper-air parameters, the climate is derived from ERA-Interim analyses for the 20-year period 1989–2008. Probabilistic skill is evaluated in this report using the continuous ranked probability skill score (CRPSS) and the area under relative operating characteristic (ROC) curve.

The continuous ranked probability score (CRPS), an integral measure of the quality of the forecast probability distribution, is computed as

$$CRPS = \int_{-\infty}^{\infty} \left[P_f(x) - P_a(x)\right]^2 dx$$

where P_f is forecast probability cumulative distribution function (CDF) and P_a is analysed value expressed as a CDF. CRPS is computed discretely following Hersbach, 2000. CRPSS is then computed as

$$CRPSS = 1 - \frac{CRPS}{CRPS_{clim}}$$

where $CRPS_{clim}$ is the CRPS of a climate forecast (based either on the ERA-Interim analysis or observed climatology). CRPSS is used to measure the long-term evolution of skill of the IFS ensemble (Figure 7) and its inter-annual variability (Figure 11).

ROC curves show how much signal can be gained from the ensemble forecast. Although a single valued forecast can be characterised by a unique false alarm (x-axis) and hit rate (y-axis), ensemble forecasts can be used to detect the signal in different ways, depending on whether the forecast user is more sensitive to the number of hits (the forecast will be issued, even if a relatively small number of members forecast the event) or of false alarms (one will then wait for a large proportion of members to forecast the event). The ROC curve simply shows the false alarm and hit rates associated with the different thresholds (proportion of members or probabilities) used, before the forecast is issued (Figure 33). Figure 33 also shows a modified ROC plot of hit rate against false alarm ratio (fraction of yes forecasts that turn out to be wrong) instead of the false alarm rate (ratio of false alarms to the total number of non-events).

Since the closer to the upper left corner (0 false alarm, 100% hits) the better, the area under the ROC curve (ROCA) is a good indication of the forecast skill (0.5 is no skill, 1 is perfect detection). Time series of the ROCA are shown in Figure 34.

The comparison of spread and skill (Figure 8 to Figure 10) takes into account the effect of finite ensemble size N by multiplying spread by the factor (N+1)/(N-1).

A. 3 Weather parameters

Verification of the deterministic precipitation forecasts is made using the newly developed SEEPS score (Rodwell et al., 2010). SEEPS (stable equitable error in probability space) uses three categories: dry, light precipitation, and heavy precipitation. Here “dry” is defined, with reference to WMO guidelines for observation reporting, to be any accumulation (rounded to the nearest 0.1 mm) that is less than or equal to 0.2 mm. To ensure that the score is applicable for any climatic region, the “light” and “heavy” categories are defined by the local climatology so that light precipitation occurs twice as often as heavy precipitation. A global 30-year climatology of SYNOP station observations is used (the resulting threshold between the light and heavy categories is generally between 3 and 15 mm for Europe, depending on location and month). SEEPS is used to compare 24-hour accumulations derived from global SYNOP observations (exchanged over the Global Telecommunication System; GTS) with values at the nearest model grid-point. 1-SEEPS is used for presentational purposes (Figure 18, Figure 19) as this provides a positively oriented skill score.

The ensemble precipitation forecasts are evaluated with the CRPSS (Figure 18, Figure 19). Verification is against the same set of SYNOP observations as used for the deterministic forecast.

For other weather parameters (Figure 20 to Figure 23), verification data are European 6-hourly SYNOP data (area boundaries are reported as part of the figure captions). Model data are interpolated to station locations using bi-linear interpolation of the four closest grid points, provided the difference between the model and true orography is less than 500 m. A crude quality control is applied to SYNOP data (maximum departure from the model forecast has to be less than 25 K, 20 g/kg or 15 m/s for temperature, specific humidity and wind speed respectively). 2 m temperatures are corrected for differences between model and true orography, using a crude constant lapse rate assumption provided the correction is less than 4 K amplitude (data are otherwise rejected).

References

Bidlot, J.-R., F. Prates, R. Ribas, A. Mueller-Quintino, M. Crepulja and Frédéric Vitart, 2020: Enhancing tropical cyclone wind forecasts, ECMWF Newsletter No. 164.

Bouallegue, Z. B., T. Haiden, and D. S. Richardson, 2018: The diagonal score: definition, properties, and interpretations. Q. J. R. Met. Soc., 144, 1463-1473.

Bouallegue, Z. B., T. Haiden, N. J. Weber, T. M. Hamill, and D. S. Richardson, 2020: Accounting for representativeness in the verification of ensemble precipitation forecasts. Mon. Wea. Rev., 148, 2049-2062.

Ferranti, L., L. Magnusson, F. Vitart and D.S. Richardson, 2018: How far in advance can we predict changes in large-scale flow leading to severe cold conditions over Europe? Q.J.R. Meteorol. Soc, 144**,** doi:10.1002/qj.3341.

Ferro, C.A.T. and D.B. Stephenson, 2011: Extremal dependence indices: improved verification measures for deterministic forecasts of rare binary events. Wea. Forecasting, 26, 699–713.

Haiden, T., I. Sandu, G. Balsamo, G. Arduini and A. Beljaars, 2018: Addressing biases in near-surface forecasts. ECMWF Newsletter No. 157, 20-25.

Haiden, T., M. Janousek, F. Vitart, L. Ferranti, and F. Prates, 2019: Evaluation of ECMWF forecasts, including the 2019 upgrade. ECMWF Technical Memorandum No. 853, 54p.

Hersbach, H., 2000: Decomposition of the Continuous Ranked Probability Score for Ensemble Prediction System. Wea. Forecasting, 15**,** 559–570.

Hólm, E., S. Lang, P. Lean and M. Bonavita, 2020: Continuous long-window data assimilation, ECMWF Newsletter No. 163, 12.

Laloyaux, P. and M. Bonavita, 2020: Improving the handling of model bias in data assimilation, ECMWF Newsletter No. 163, 18–22.

Matthes, K., B. Funke, M. Anderson, L. Barnard, J. Beer, P. Charbonneau et al., 2017: Solar forcing for CMIP6 (v3. 2), Geoscientific Model Development, 10, 2247–2302.

Moody, E. G., M. D. King, C.B. Schaaf, D.K. Hall and S. Platnick, 2007: Northern Hemisphere five-year average (2000–2004) spectral albedos of surfaces in the presence of snow: Statistics computed from Terra MODIS land products, Remote Sensing of Environment, 111, 337–345.

Polichtchouk, I., M. Diamantakis and F. Váňa, 2020: Quintic vertical interpolation improves forecasts of the stratosphere, ECMWF Newsletter No. 163, 23–26.

Rodwell, M. J., D.S. Richardson, T.D. Hewson and T. Haiden, 2010: A new equitable score suitable for verifying precipitation in numerical weather prediction. Q. J. R. Meteorol. Soc., 136**,** 1344–1363.

Sandu, I., T. Haiden, G. Balsamo, P. Schmederer, G. Arduini, J. Day, A. Beljaars, Z. Ben Bouallegue, S. Boussetta, M. Leutbecher, L. Magnusson, and P. de Rosnay, 2020: Addressing near-surface forecast biases: outcomes of the ECMWF project 'Understanding uncertainties in surface atmosphere exchange' (USURF). ECMWF Technical Memorandum No. 875, 43p.

Schaaf, C.B., F. Gao, A.H. Strahler, W. Lucht, X. Li, Xiaowen, T. Tsang et al., 2002: First operational BRDF, albedo nadir reflectance products from MODIS. Remote sensing of Environment, 83, 135–148.

Schmederer, P., I. Sandu, T. Haiden, A. Beljaars, M. Leutbecher, and C. Becker, 2019: Use of super-site observations to evaluate near surface temperature forecasts. ECMWF Newsletter No. 161, 32-38.

Sleigh, M., P. Browne, C. Burrows, M. Leutbecher, T. Haiden, and D. Richardson, 2020: IFS upgrade greatly improves forecasts in the stratosphere. ECMWF Newsletter No. 164, 18-23.